Please find the published version at: https://doi.org/10.1016/j.applthermaleng.2020.116148

Polydispersed Droplet Spectrum and Exergy Analysis in Wet Steam Flows using Method of Moments

Hongbing Ding[1], Yuhe Tian[1], Chuang Wen[2], Chao Wang[1, *], Chunqian Sun[1]

[1]Tianjin Key Laboratory of Process Measurement and Control, School of Electrical and Information Engineering, Tianjin University, Tianjin 300072, China

[2]Faculty of Engineering, University of Nottingham, University Park, Nottingham NG7 2RD, UK

*Corresponding author: Chao Wang, Email: wangchao@tju.edu.cn

Abstract:

In steam turbine flow, the complex droplet spectrum caused by nonequilibrium condensation is necessary to be modeled accurately to predict the droplet behavior and estimate the exergy destruction and erosion rate. This study built and validated a polydispersed model with Quadrature method of moments (QMOM), consisting of transition SST model, the moments and entropy generation. A spline-based algorithm was used to reconstruct the shape of the probability density function (PDF) of radius. It's proved that the polydispersed model has a better prediction result for Sauter radius compare with monodispersed model. Then, the distributions of moments and droplet spectra in the nozzle with effects of asymmetric lambda shock and evaporation were investigated. The shape of droplet spectrum is closer to gamma distribution in nucleation zone and log-normal distribution in growth zone when outflow is supersonic. In the turbine, because the oblique shock induces complex evaporation and secondary condensation, the reconstructed shape is closer to gamma distribution. Finally, the obtained maximum exergy destruction is 25.293 kJ/kg. The rate of exergy destruction increases from 1.04% to 4.45%. The range of Baumann factor is 0.574~1.312. Besides, the erosion rate in polydispersed model is only 58.4%~64.3% of monodispersed model. The polydispersed model used in this study can predict the droplet spectrum and energy loss of the turbine systems more accurately.

Keywords: Nonequilibrium condensation; steam turbine; Polydispersed droplet spectrum; QMOM; Exergy destruction; Erosion rate

Nomenclature

a	shape parameter
a_B	Baumann factor, -
A	area, m^2
C_V	coefficient of variation, -
c_p	specific heat capacity, $J\cdot kg^{-1}\cdot K$
d	throat diameter, m
Er	erosion rate, mm h^{-1}
e_D	specific exergy destruction, $J\cdot kg^{-1}$
e_x	specific exergy, $J\cdot kg^{-1}$
$F(r)$	droplet number density function, m^{-1} kg^{-1}
$f(r)$	PDF of droplet size, m^{-1}
$\hat{f}(\hat{r})$	PDF of normalized radius, -
$G(r)$	growth rate of the droplet, m s^{-1}
h	static enthalpy, $J\cdot kg^{-1}$
h_{lv}	latent heat, $J\cdot kg^{-1}$
I	nucleation rate, $m^{-3}\cdot s^{-1}$
K_b	Boltzmann constant, 1.38×10^{-23} $J\cdot K^{-1}$
Kn	Knudsen number, -
k	turbulence kinetic energy, $J\cdot kg^{-1}$
Ma	Mach number, -
m_l	droplet mass flow flux, kg mm^2 h^{-1}
m_v	mass change rate, $kg\cdot m^{-3}\cdot s^{-1}$
m_m	water molecule mass, 2.99×10^{-26} kg
Pr	Prandtl number, -
p	fluid pressure, Pa
q_c	coefficient of condensation, -
q_m	mass flow rate, $kg\cdot s^{-1}$
$Re_{\theta t}$	transition Reynolds number, -
R_v	specific gas constant of vapor, $J\cdot kg^{-1}\cdot K^{-1}$
r	radius, m
$\hat{r}$	normalized radius, $= r/r_{10} = r/(\mu_1/\mu_0)$
S_s	supersaturation ratio, p/p_s
S	spline function, $S(r)$
s	specific entropy, $J\cdot kg^{-1}\cdot K^{-1}$
T	fluid temperature, K
Tu	turbulence intensity, -
t	time, s

Greek

α	volume fraction, -
β	wetness fraction, -
Γ	gamma function
γ	intermittency, -
γ_v	specific heat ratio, -
ΔT	degree of subcooling, $T_s(p_v)$-T_v, K
δ	dirac delta function
ζ_D	exergy destruction ratio, -
η	dynamic viscosity, $Pa\cdot s$
η_{wet}	wet isentropic efficiency, -
θ	Kantrowitz correction coefficient, -
λ	thermal conductivity, $W\cdot m^{-1}\cdot K^{-1}$
μ_k	k-th order moment
$\hat{\mu}_k$	normalized moments, -
ξ_η	efficiency ratio, -
ρ_m	density of mixture, $kg\cdot m^{-3}$
σ	surface tension of liquid, $N\cdot m^{-1}$
υ_i	eigen vectors
μ	specific dissipation rate, s^{-1}

Subscripts

0	dead state
eff	effective parameter
c	critical
d	destruction
dry/wet	dry gas/wet gas
gen	generation
in, out	inflow, outflow
i	abscissa and weight order
j	tensor notation
k	moment order
l	liquid
m	mixture
s	saturation state
t	turbulent flow
$tran$	transfer

U	local velocity magnitude, m·s^{-1}	v	vapor
u_i	velocity component, m·s^{-1}	w	Wilson point
V	volume, m^3		
w	quadrature weight, # kg^{-1}	Superscripts	
$\hat{w}$	normalized weight, -	‘	fluctuation
x, y	cartesian coordinate, m	-	mean
Y	rate of entropy generation, J K^{-1}·m^{-3}·s^{-1}	*	at stagnation condition
y^+	yplus		

1. Introduction

Energy is the base of modern economic development and power industry is the pillar industry of energy. The main equipment of modern thermal power plant is steam turbine [1] which allows wet-steam flow with nonequilibrium condensation in the low-pressure stages, and droplets cause thermal efficiency reduction [2], additional energy losses [3], entropy generation [4-5] and erode the surfaces of blade [6-7]. The non-equilibrium condensation is exceedingly complicated, including the interference between condensation pseudo-shock and the aerodynamic shock, unsteady flows and separation of boundary layer [8,9]. In order to obtain more accurate data and results, thermodynamic analysis of power plant performance must be performed [10]. The behaviour of wet steam flow in turbine can assess through droplet spectra [11]. In addition, the droplet size distribution provides fundamental information for turbine designers to minimize the effect of wet steam on the turbine [12].

Many experimental studies about the influence of droplet size on turbines were reported for decades. Tatsuno and Nagao [13] used the forward scattering method to measure the average droplet size at the outlet of last stage blade. Ahmad et al. [14] found through experiments that the erosion of turbine blade will grow as increasing sizes of droplet. Wang et al. [15] measured water droplet diameter behind the blade of the last stage using the total light scattering technique. Tabakoff et al. [16] studied the erosion law and erosion intensity of blade surfaces in the case of uneven and uniform particle distribution. Alekseev et al. [17] used particle tracking velocimetry PTV to investigate the polydispersed wet steam flow in the turbine. Filippov et al. [18] conducted some experiments for studying the motion of the droplet inside the turbine based on laser diagnostic instrument.

Recently, Computational Fluid Dynamics (CFD) as a method of analyzing condensation phenomenon in wet steam flow is popular with an increasing number of scholars. And CFD is considered as an excellent way for studying experiments with high costs and accurate equipment [19]. The condensed phase can be solved by two methods, namely Lagrangian [20] and Eulerian schemes [21]. For calculating the liquid phase, wet steam model can be divided into a single-fluid model (SFM) with no-slip of interphase, and a two-fluid model (TFM) considering the interphase slip velocity [22]. Wróblewski and Dykas [23] built the TFM to observe the velocity slip and found the maximum of slip velocity is 1.3 m s^{-1}. However, the viscous effect is not considered in this TFM. Abadi et al. [24] carried out a two-fluid model to observe non-equilibrium condensation in high-pressure nozzles. Han et al. [25] built a TFM model to evaluate the aerodynamic and dehumidification performances of turbine stator when the endwall fences is heating. But actually, most scholars built the SFM for wet steam flow within the nozzle and turbine due the slip effect is tiny. White and Young [26] put forward a single-fluid model for vapor condensation at low pressure. Starzmann et al. [27] found the diameters of condensed droplets in steam turbine are less than 0.5 μm so that the slip between two phases be neglected. Yang et al. [28] built the SFM for wet steam flow to analyze the intricate feature of vapor condensation inside supersonic ejector. Zhang et al. [29-31] proposed a modified SFM model for numerically studying the dehumidification structure optimization of steam turbine. Edathol et al. [32] built an E-E mixture model based on a pressure-based solver for non-equilibrium condensation.

Many works focused on the droplet spectrum. The radius of droplet has a crucial effect on the calculation of heat transfer and phase change between vapor and liquid phase [33]. There are usually two kind methods for modeling the liquid droplet phase in wet steam flow [34]. One is a monodispersed model (Mono) and the other is a polydispersed model. The monodispersed model, although simple to calculate, cannot predict the effect of droplet size distribution. Therefore, the polydispersed model is better to be employed in the study of polydispersed wet steam flow within turbine blade.

There are many methods for modeling polydispersed liquid phase, including the method of a finite number of droplet groups with Lagrangian approach, the method of a finite number of droplet fixed-volume bins with Eulerian approach, spectrum pruning method, the method of moment (MOM), the quadrature method of moment (QMOM) [35]. White and Young [26] discretize the droplet distribution into several droplet groups. Gerber and Kermani [36] studied a finite number of droplet fixed-volume bins method and used a conservation fixed-volume integration to discretize conservation equations of the liquid and gas phase. Aliabadi et al. [7] proposed a new method with dividing the nucleation zone into twenty parts to generate 20 droplet groups. However, it is difficult to give a criterion for selecting the number of droplet groups or droplet fixed-volume bines and determining the nucleating timestep or space interval. White [33] and Gerber [37] investigated MOM and QMOM for polydispersed droplets and predicted distribution of droplets along with length of nozzle. Hughes et al. [11] studied the spectrum pruning method and QMOM to reduce the droplet groups number. Afzalifar et al. [38] found the method of moments only solves several transport equations of droplet sizes which can reduce computational time and QMOM method is a better choose to predict the effect of droplet size distribution.

Besides, for MOM and QMOM, the droplet spectrum, namely droplet number density distribution also can be reconstructed through several moments. Hulburt and Stanley [39] assumed the particle size spectrum has a certain empirical form and then was reconstructed by using low-order moments. Diemer and Olson [40] proposed a nonlinear regression technique to reconstruct the droplet spectrum from the moments based on a prior shape. John et al. [41] presented a discrete method for reconstructing droplet distribution using the moments. However, the discrete method only applies to simple reconstruction. Souza et.al. [42] improved the PDF reconstruction algorithm by using the spline function with an adaptive algorithm. By using splines without prior knowledge can reconstruct droplet distribution with a finite number of moments quickly.

In addition to energy, exergy analysis is an effective method to evaluate the performance of power plants [43]. However, few researchers have analyzed the droplet spectrum, exergy destruction and erosion rate in wet steam turbine based on polydispersed model with QMOM approach. In present work, a polydispersed viscous wet steam model was built. The droplet nucleation and growth were described by the moments of lower orders of droplet number density based on QMOM. The droplet spectrum was reconstructed by using spline-based algorithm from a finite number of moments. Then, the moments distributions and droplet spectra of nonequilibrium condensation flow within the nozzle and turbine were analyzed. Finally, the entropy, exergy, Baumann factor and erosion rate were computed to provide an effective information for improve turbine efficiency and reduce energy losses.

2. **Polydispersed model**

The wet steam flow with homogeneous condensation was investigated by using the compressible turbulent fluid model. It is assumed that the droplets are spherical and polydisperse, as shown in Fig. 1. The integral of droplet number density distribution can be replaced by first 2*m* moments (μ_k, for k =0 through 2*m*-1, where 2*m* represents the number of moments) of distribution based on QMOM. The velocity slip between the vapor and droplet can be negligible (of order 0.1 m s^{-1}) because the droplet size of homogenous condensation is submicron and the maximum velocity slip is only about 1 m s^{-1} [22]. Thus, the effect of condensation-induced droplets on turbulence can be neglected. The mixture density is $\rho_m = \alpha_v\rho_v + \alpha_l\rho_l$. The volume fraction of liquid fraction is $\alpha_l = V_l/V_m$. $\alpha_v + \alpha_l = 1$. ρ_v and ρ_l are densities of vapor and liquid phases. The wetness fraction, namely liquid mass fraction is $\beta = \alpha\rho_l/\rho_m$.

Fig. 1 Polydisperse and monodispersed models for wet steam flows with homogeneous condensation.

2.1. Quadrature method of moments (QMOM)

Hulburt and Katz [39] introduced MOM of droplet number density function to describe droplet growth and nucleation. McGraw [44] proposed Quadrature Method of Moments (QMOM) with a few droplet size moments for polydispersed wet steam flow. QMOM possesses very high accuracy and efficiency which requires neither a restricted growth law nor assuming a mathematical form for droplet number distribution. The droplet number density function $F(r, x_i, t)$ is expressed as

$$\frac{\partial \rho_m F}{\partial t} + \frac{\partial}{\partial x_j}\left(\rho_m F u_j\right) + \frac{\partial}{\partial r}\left(\rho_m F G\right) = I\delta\left(r - r_c\right) \tag{1}$$

where, Fdr represents droplet number in the interval [r, r+dr] per unit mass. $G(r)$ represents growth rate which is dependent on the droplet size. j is tensor notation. I and u_j represent nucleation rate and mean velocity component, respectively. δ is Dirac delta function.

The k-th order moment of number density is expressed by:

$$\mu_k = \int_0^\infty r^k F\left(r\right) dr,\ k = 0,1,2,... \tag{2}$$

where, μ_0 (kg^{-1}) means the droplets number per unit mass of mixture. μ_2 (m^2 kg^{-1}) is the sum of surface of droplets per unit mass. μ_3 (m^3 kg^{-1}) is the sum of volumes of droplets per unit mass. The number-average radius r_{10} is equal to μ_1/μ_0. The volume-surface-average or Sauter radius r_{32} is equal to μ_3/μ_2.

Thus, the wetness fraction is calculated by

$$\beta = \int_0^\infty \frac{4\pi}{3}\pi\rho_l r^3 F\left(r\right) dr = \frac{4\pi}{3}\rho_l \mu_3 \tag{3}$$

Combined with Eqs. (1) and (2), the transport equations for the moments of droplet number density are expressed as

$$\frac{\partial \rho_m \mu_k}{\partial t} + \frac{\partial}{\partial x_j}\left(\rho_m \mu_k u_j\right) = k\int_0^{\infty} r^{k-1} \rho_m G F dr + I r_c^k \tag{4}$$

The integral in right side of Eq. (4) is calculated by a sum using weights (w_i) and abscissa (r_i) derived from m-point Gaussian quadrature by McGraw [44], and is expressed by

$$\frac{\partial \rho_m \mu_k}{\partial t} + \frac{\partial}{\partial x_j}\left(\rho_m \mu_k u_j\right) = k \rho_m \sum_{i=1}^{m} r_i^{k-1} G\left(r_i\right) w_i + I r_c^k \tag{5}$$

The moments are re-written as

$$\mu_k = \int_0^{\infty} r^k F\left(r\right) dr = \sum_{i=1}^{m} r_i^k w_i \tag{6}$$

where the dimension of w_i is kg^{-1}.

It is found that the first 2m moments where k = 0 ~ 2m-1 can calculate m weights w_i and abscissa r_i. In the study, m = 3 is chosen. Thus, 3 quadrature weights and abscissas determined from 6 moments using the product-difference (PD) algorithm [45]. The symmetric tridiagonal matrix of PD algorithm is

$$\mathrm{J}_3 = \begin{bmatrix} a_1 & b_1 & \\ b_1 & a_2 & b_2 \\ & b_2 & a_3 \end{bmatrix} \tag{7}$$

where,

$$\begin{aligned}
& a_1 = \mu_1 \ , \quad b_1^2 = \mu_2 - \mu_1^2 \\
& a_2 = \left(\mu_1^3 - 2\mu_1\mu_2 + \mu_3\right) / \left(\mu_2 - \mu_1^2\right) \\
& b_2^2 = \left(-\mu_2^3 + 2\mu_1\mu_2\mu_3 - \mu_3^2 - \mu_1^2\mu_4 + \mu_2\mu_4\right) / \left(\mu_2 - \mu_1^2\right)^2 \\
& a_3 = \frac{\mu_1\left(-\mu_2^3 + 2\mu_1\mu_2\mu_3 - \mu_3^2 - \mu_1^2\mu_4 + \mu_2\mu_4\right)}{\left(\mu_1\mu_3 - \mu_2^2\right)\left(\mu_2 - \mu_1^2\right)} + \frac{\left(\mu_2 - \mu_1^2\right)\left(-\mu_3^3 + 2\mu_2\mu_3\mu_4 - \mu_1\mu_4^2 - \mu_2\mu_5^2 + \mu_1\mu_3\mu_5\right)}{\left(-\mu_2^3 + 2\mu_1\mu_2\mu_3 - \mu_3^2 - \mu_1^2\mu_4 + \mu_2\mu_4\right)\left(\mu_1\mu_3 - \mu_2^2\right)}
\end{aligned} \tag{8}$$

Then, the values of abscissas r_i are the eigenvalues of J_3. The weights w_i are calculated by the eigen vectors υ_{i1}, as follows,

$$w_i = \mu_0 \upsilon_{i1}^2 \tag{9}$$

2.2. Nucleation and droplet growth

In this study, homogeneous nucleation rate I (m^{-3}·s^{-1}) is calculated by [46]

$$I = \frac{q_c}{1+\theta}\left(\frac{2\sigma}{\pi m_m^3}\right)^{1/2} \frac{\rho_v^2}{\rho_l} \exp\left(-\frac{4\pi r_c^2 \sigma}{3 K_b T_v}\right) \tag{10}$$

where, q_c is the condensation coefficient. m_m is single water molecule mass. σ is surface tension. K_b and T_v are Boltzmann constant and vapor temperature. Kantrowitz correction coefficient θ is

$$\theta = 2\frac{\gamma_v - 1}{\gamma_v + 1}\frac{h_{lv}}{R_v T_v}\left(\frac{h_{lv}}{R_v T_v} - \frac{1}{2}\right) \tag{11}$$

where, h_{lv} and R_v are latent heat of phase change and specific gas constant. The liquid surface tension σ is expressed as

$$\sigma = a_1\left(\frac{T_c - T}{T_c}\right)^{a_2}\left[1 + a_3\left(\frac{T_c - T}{T_c}\right)\right] \tag{12}$$

where a_1 = 0.2358 N m^{-1}; a_2 = 1.256; a_3 = -0.625. The vapor critical temperature T_c =647.15 K. [47]. The critical radius of nucleation is computed by

$$r_c = \frac{2\sigma}{\rho_l R_v T_v \ln S_s} \tag{13}$$

where, S_s denotes the supersaturation ratio defined as the ratio of vapor pressure to saturation pressure, = p/p_s.

The droplet growth rate $G(r)$ related to radius r is [62]

$$G(r) = \frac{dr}{dt} = \frac{\lambda_v (T_l - T_v)}{\rho_l h_{lv} r \left(\frac{1}{1+2\beta_0 \mathrm{Kn}} + 3.78(1-v)\mathrm{Kn}/\mathrm{Pr} \right)} \tag{14}$$

where β_0 =2.0 and v is equal to

$$v = \frac{R_v T_s}{h_{lv}} \left(\alpha_0 - 0.5 - \frac{2-q_c}{2q_c} \left(\frac{\gamma_v + 1}{2\gamma_v} \right) \frac{c_p T_s}{h_{lv}} \right) \tag{15}$$

where α_0 = 9. Knudsen number Kn is [63]

$$\mathrm{Kn}(r) = \frac{3\eta_v \sqrt{R_v T_v}}{4 p_v r} \tag{16}$$

where η_v is dynamic viscosity of vapor. The droplet surface temperature T_l is [64]

$$T_l = T_s(p_v) - \Delta T \frac{r_c}{r} \tag{17}$$

where, ΔT denotes degree of subcooling, $T_s(p_v)$-T_v. T_s represents saturation temperature.

The mass change rate m_v (kg·m^{-3}·s^{-1}), which can be derived from Eqs.(14)-(17) is the mass source for governing equations and can be computed by,

$$m_v = \frac{4}{3}\pi\rho_l I r^{*3} + 4\pi\rho_l \rho_m \int_0^\infty r^2 G F dr = \frac{4}{3}\pi\rho_l I r^{*3} + 4\pi\rho_l \rho_m \sum_{i=1}^{m} G(r_i) r_i^2 w_i \tag{18}$$

2.3. Vapor phase turbulent model

The continuity equation of vapor phase can be calculated by

$$\frac{\partial(\alpha_v \rho_v)}{\partial t} + \frac{\partial}{\partial x_j}(\alpha_v \rho_v u_j) = -m_v \tag{19}$$

The momentum balance for vapor phase is

$$\frac{\partial(\alpha_v \rho_v u_i)}{\partial t} + \frac{\partial}{\partial x_j}(\alpha_v \rho_v u_i u_j) = -\alpha_v \frac{\partial p_v}{\partial x_i} + \frac{\partial}{\partial x_j}\left[\alpha_v \eta_v \left(\frac{\partial u_j}{\partial x_i} + \frac{\partial u_i}{\partial x_j} - \frac{2}{3}\delta_{ij} \frac{\partial u_l}{\partial x_l} \right) \right] + \frac{\partial}{\partial x_j}\left(-\alpha_v \rho_v \overline{u_i' u_j'} \right) - m_v u_i \tag{20}$$

where δ_{ij} and u_i' denotethe Kronecker delta and velocity fluctuating component. Reynolds stresses $-\rho_v \overline{u_i' u_j'}$ is related to the turbulent viscosity η_t and turbulence kinetic energy k. The energy conservation equation for vapor phase is

$$\frac{\partial \alpha_v \rho_v E_v}{\partial t} + \frac{\partial}{\partial x_j}\left[u_j (\alpha_v \rho_v E_v + p_v) \right] = \frac{\partial}{\partial x_j}\left[\alpha_v \left(\lambda_v + \frac{c_{p,v}\eta_t}{Pr_t} \right) \frac{\partial T_v}{\partial x_j} + \alpha_v u_i (\tau_{ij})_{eff} \right] - m_v (h_v - h_{lv}) \tag{21}$$

where, total energy is $E_v = h_v - \frac{p_v}{\rho_v} + \frac{1}{2}u_i u_i$. $(\tau_{ij})_{eff}$ is the deviatoric stress tensor. The turbulent viscosity η_t is computed by

$$\eta_t = \frac{\rho_v k}{\omega}\frac{1}{\max\left[\frac{1}{\alpha^*}, \frac{\Omega F_2}{a_1\omega}\right]} \tag{22}$$

The transition SST model are modelled by

$$\begin{aligned}
&\frac{\partial}{\partial t}(\rho_v k) + \frac{\partial}{\partial x_j}(\rho_v k u_j) = \frac{\partial}{\partial x_j}\left[\left(\eta + \frac{\eta_t}{\sigma_k}\right)\frac{\partial k}{\partial x_j}\right] + G_k - Y_k \\
&\frac{\partial(\rho_v\omega)}{\partial t} + \frac{\partial}{\partial x_j}(\rho\omega u_j) = \frac{\partial}{\partial x_j}\left[\left(\eta + \frac{\eta_t}{\sigma_\omega}\right)\frac{\partial \omega}{\partial x_j}\right] + G_\omega - Y_\omega + D_\omega
\end{aligned} \tag{23}$$

The intermittency γ and transition momentum-thickness $Re_{\theta t}$ are as follow

$$\begin{aligned}
&\frac{\partial(\rho_v\gamma)}{\partial t} + \frac{\partial(\rho_v u_j \gamma)}{\partial x_j} = P_{\gamma 1} - E_{\gamma 1} + P_{\gamma 2} - E_{\gamma 2} + \frac{\partial}{\partial x_j}\left[\left(\eta + \frac{\eta_t}{\sigma_\gamma}\right)\frac{\partial \gamma}{\partial x_j}\right] \\
&\frac{\partial(\rho_v Re_{\theta t})}{\partial t} + \frac{\partial(\rho_v u_j Re_{\theta t})}{\partial x_j} = P_{\theta t} + \frac{\partial}{\partial x_j}\left[\sigma_{\theta t}(\eta + \eta_t)\frac{\partial Re_{\theta t}}{\partial x_j}\right]
\end{aligned} \tag{24}$$

where, variables in Eqs. (22)-(24) were defined in our previous work [46].

2.4. Exergy destruction and erosion rate

2.4.1. Entropy generation of phase change

Redlich-Kwong EOS for the vapor is expressed as

$$p = \frac{RT}{V' - b} - \frac{\alpha_0}{V'(V' + b)T_r^{0.5}} \tag{25}$$

where, R and V' are universal gas constant and specific molar volume (m^3 kmol^{-1}). T_r is the reduced temperature. The vapor isobaric specific heat capacity is [48]

$$c_{p(v)} = 1563.077 + 1.603755T_v - 0.002932784T_v^2 + 3.216101e\text{-}6T_v^3 - 1.156827e\text{-}9T_v^4 \tag{26}$$

The liquid isobaric specific heat capacity is

$$c_{p(l)} = -36571.6 + T_l\left(555.217 + T_l\left(-2.96724 + T_l\left(0.00778551 + T_l\left(-1.00561\text{e-}5 + 5.14336\text{E-}9T_l\right)\right)\right)\right) \tag{27}$$

For wet steam, the specific entropy s is defined as

$$s = \beta s_l + (1-\beta)s_g \tag{28}$$

In our previous study [46], the local specific entropy change of wet steam is defined as

$$s - s_{\text{in}}^* = s_{tran} + s_{gen} = s_{tran} + s_{gen,D} + s_{gen,C} + s_{gen,L} + s_{gen,A} \tag{29}$$

where s_{tran} denotes the entropy transfer. s_{gen} is the total entropy generation which can be divided into 4 parts, namely $s_{gen,D}$, $s_{gen,C}$, $s_{gen,L}$ and $s_{gen,A}$ attributing to viscous dissipation, heat transfer, phase change and aerodynamic loss, respectively.

Both viscous dissipation and heat transfer also have two groups, mean and fluctuating quantities, i.e.

$s_{gen,D} = s_{gen,\overline{D}} + s_{gen,D'}$ and $s_{gen,C} = s_{gen,\overline{C}} + s_{gen,C'}$. The transport equation of each part of entropy generation in Mono method has been presented in Ref [46]. The source term expressions (Eqs. (30)-(34)) of entrophy generation equations in QMOM method are the same as the Mono method, except for entropy generation due to condensation phase change which is sensitive to droplet size distribution.

$$Y_{tran} = \frac{\partial}{\partial x_i}\left(\frac{\lambda_{eff}}{T}\frac{\partial T}{\partial x_i}\right) \tag{30}$$

$$Y_{Gen,\overline{D}} = \frac{2\mu S_{i,j} S_{i,j}}{T} \tag{31}$$

$$Y_{Gen,D'} = \frac{\rho\beta^* k\omega}{T}, \beta^* = 0.09 \tag{32}$$

$$Y_{Gen,\overline{C}} = \frac{\lambda}{T^2}\frac{\partial T}{\partial x_i}\frac{\partial T}{\partial x_i} \tag{33}$$

$$Y_{Gen,C'} = \frac{\alpha_t}{\alpha_0} Y_{Gen,C'} = \frac{\alpha_t}{\alpha_0}\frac{\lambda}{T^2}\frac{\partial T}{\partial x_i}\frac{\partial T}{\partial x_i} \tag{34}$$

where, the mean strain rate $S_{i,j} = \frac{1}{2}\left(\frac{\partial u_j}{\partial x_i} + \frac{\partial u_i}{\partial x_j}\right)$. α_t is turbulent thermal diffusivity.

In polydispesed model, the entropy generation $s_{gen,L}$ due to phase change including condensation and evaporation processes is dependent on the temperature difference between liquid and vapor phases, as follows [49]

$$\frac{\partial \rho_m s_{gen,L}}{\partial t} + \frac{\partial}{\partial x_i}\left(\rho_m s_{gen,L}\, u_i\right) = Y_L \tag{35}$$

where, the source term, local entropy generation rate Y_L is calculated by

$$Y_L = 4\pi\rho_m h_{lv}\int_0^\infty \rho_l r^2 GF\left(\frac{1}{T_v} - \frac{1}{T_l(r)}\right)dr = 4\pi\rho_m h_{lv}\sum_{i=1}^{m}\rho_l G(r_i) r_i^2 w_i\left(\frac{1}{T_v} - \frac{1}{T_l(r_i)}\right) \tag{36}$$

2.4.2. Exergy destruction ratio

The specific flow exergy e_x can be derived from exergy rate balance equation for the steady open system and can be described by [50]

$$e_x = h - h_0 - T_0\left(s - s_0\right) + \frac{U^2}{2} \tag{37}$$

where the subscript '0' represents dead state or reference environment. The environment pressure p_0 is 3.14 kPa as the same as the steam condenser and temperature T_0 is 298 K [51]. Thus, s_{v0} = 0 kJ·kg^{-1} K^{-1} and s_{l0} = -8.193 kJ·kg^{-1} K^{-1}. In addition, the specific exergy destruction e_D is calculated by

$$e_D = \Delta e_x = T_0 s_{gen} \tag{38}$$

The exergy destruction rate E_D (kW) is expressed as

$$E_D = q_m e_D \tag{39}$$

where q_m represents mass flow rate. Then, the exergy destruction ratio ζ_D is expressed as [52]

$$\zeta_D = \frac{e_D}{e_{x,\text{in}}} = \frac{T_0 s_{gen}}{h^*_{\text{in}} - h_0 - T_0\left(s^*_{\text{in}} - s_0\right)} \tag{40}$$

2.4.3. Baumann factor and erosion rate

The efficiency ratio ξ_η of turbine can be calculated by

$$\xi_\eta = \frac{\eta_{\mathrm{wet}}}{\eta_{\mathrm{dry}}} = \frac{1-\zeta_{D,\mathrm{wet}}}{1-\zeta_{D,\mathrm{dry}}} = 1 - a_B \beta_{\mathrm{m}} \tag{41}$$

where, a_B is Baumann factor. β_{m} is equal to a half of mass-weighted average outlet wetness fraction $0.5y_{\mathrm{out}}$ which is taken into account the partial dry expansion with non-equilibrium condensation in this single stage [3]. η_{wet} and η_{dry} are wet total isentropic efficiency and dry isentropic efficiency, respectively. The isentropic efficiency is calculated by [65]

$$\eta_{\mathrm{dry}} = \frac{h_{in} - h_{out}}{h_{in} - h_{out,is}} \tag{42}$$

where subscript 'is' represents the isentropic condition and h is the specific enthalpy of steam.

Besides, the moving droplets colliding with turbine blades result in the erosion of blades and influence the safety and reliability of turbine operation [53]. Ahmad indicated that, the erosion damage of a single 500 μm droplet is far more serious than damages of 125 droplets with 100 μm diameter. It is found that droplet radius is main factor on turbine erosion. The blade erosion derived by Lee [54] is expressed as

$$Er = k_e \left(\frac{m_l}{m_{ref}}\right)\left(\frac{U_l}{U_{ref}}\right)^{5.1}\left(\frac{r}{r_{ref}}\right)^{b} 10^{\gamma_c H_v} \tag{43}$$

where k_e is the corrosion constant and m_l is the droplet mass flow flux, kg mm^2 h^{-1}. U_l and r represent the droplet velocity and radius. b is between 2 and 4.5. γ_c and H_v represent a hardness constant and Vickers hardness value. According to erosion model of Lee, the erosion rate is related to water droplet radius and wetness fraction,

$$Er \propto \beta r^b \tag{44}$$

In this study, the parameter $b = 2$, the normalized local erosion rate $\hat{E}r$ is defined as

$$\hat{E}r_{avg} = \frac{\beta r^2}{\beta_{\mathrm{ref}} r_{\mathrm{ref}}^2} \tag{45}$$

where, the reference parameter β_{ref} and r_{ref} are equal to 0.01 and 1e-7 m.

For polydisperse droplets, the normalized local erosion rate $\hat{E}r_{QMOM}$ is defined as

$$\hat{E}r_{QMOM} = \frac{\int_0^\infty \frac{4\pi}{3}\pi\rho_l r^3 r^2 F(r)\,dr}{\beta_{\mathrm{ref}} r_{\mathrm{ref}}^2} = \frac{\frac{4\pi}{3}\rho_l \mu_5}{\beta_{\mathrm{ref}} r_{\mathrm{ref}}^2} \tag{46}$$

Thus, the mass-weighted average of normalized erosion rate $\overline{\hat{E}r}_{QMOM}$ at the outlet is

$$\overline{\hat{E}r}_{QMOM} = \frac{4\pi}{3}\rho_l \bar{\mu}_5 \Big/ \left(\beta_{\mathrm{ref}} r_{\mathrm{ref}}^2\right) \tag{47}$$

where, the mass-weighted average of a quantity ϕ at outlet is defined as follows:

$$\bar{\phi} = \frac{\int \phi\rho\vec{U}\cdot d\vec{A}}{\int \rho\vec{U}\cdot d\vec{A}} = \frac{\sum_{i=1}^{N}\phi_i\rho_i\left|\vec{U}_i\cdot\vec{A}_i\right|}{\sum_{i=1}^{N}\rho_i\left|\vec{U}_i\cdot\vec{A}_i\right|} \tag{48}$$

where A and U denote facet area and local velocity, respectively. N is the total number of facets.

3. **Reconstruction algorithm for distribution**

3.1. Spline-based reconstruction algorithm

Actually, the droplet spectra, namely droplet size distribution $f(r)$ can also be reconstructed if a finite number of moments are known. The usual method is to use a priori knowledge concerning the shape of probability density function (PDF), such as Gauss distribution, log-normal distribution and gamma distribution. The Gaussian normal distribution is expressed as

$$f(r) = \frac{1}{\sigma_g \sqrt{2\pi}} \exp\left(-\frac{(r - r_{10})^2}{2\sigma_g^{\,2}} \right) \tag{49}$$

where the mean radius $r_{10} = \mu_1/\mu_0$, and standard deviation $\sigma_g = \sqrt{\frac{\mu_2}{\mu_0} - \left(\frac{\mu_1}{\mu_0}\right)^2} = r_{10}\sqrt{\frac{\mu_0\mu_2}{\mu_1^{\,2}} - 1} = r_{10}C_V$. C_V is coefficient of variation.

Log-normal distribution is

$$f(r) = \frac{1}{r\sigma_{\log}\sqrt{2\pi}} \exp\left(-\frac{(\ln r - \ln r_{\log})^2}{2\sigma_{\log}^{\,2}} \right) \tag{50}$$

where, the median $r_{\log} = r_{10}\exp\left(-0.5\sigma_{\log}^{\,2}\right)$, and $\sigma_{\log} = \sqrt{\ln\frac{\mu_0\mu_2}{\mu_1^{\,2}}}$. $\sigma_{\log}$ is shape parameter (standard deviation of the log-normal function), $r_{\log}$ is the location parameter. Mode (the most probable value) is equal to $r_{10}\exp\left(-1.5\sigma_{\log}^{\,2}\right)$ which is smaller than mean radius r_{10}.

Gamma distribution is expressed as

$$f(r) = \frac{1}{b^a \Gamma(a)} r^{a-1} \exp\left(-\frac{r}{b}\right), a > 0 \tag{51}$$

Where a and b denote the shape and scale parameters. $a = r_{10}^2/\sigma_g^2 = 1/C_V^2$ and $b = \sigma_g^2/r_{10}$. In this study, $a>1$. $\Gamma(a)$ is gamma function, $= \int_0^\infty z^{a-1}\exp(-z)\,dz$. The mode radius is $(a-1)b = r_{10} - \sigma_g^2/r_{10}$ where PDF reaches a maximum $f(r)$. Median has no simple closed form.

The known moments are only used to fit parameters for PDF. Nevertheless, it is restricted that PDF should have a simple shape. A reconstruction algorithm by using low-order splines can be utilized to solve this problem [41]. PDF shape is approximated by using a piecewise polynomial function. Thus, no priori assumptions about PDF shape are required.

Let $\{r_1 < r_2 < r_3 < \cdot\cdot\cdot < r_{n+1}\}$ be a set of given knots with $a = r_1 < r_2 < r_3 < \cdot\cdot\cdot < r_{n+1} < b$. $S^{(L)}(r)$ of degree l on [a, b] is a piecewise polynomial spline. $S_i(r)$ is the spline with subinterval $[r_i, r_{i+1}]$, $i = 1, \ldots,$ n. It has $n + 1$ knots, consequently n intervals and $(l+1)n$ unknowns.

Ansatz for piecewise polynomials are defined as

$$f(r) \approx S_i(r) = \sum_{j=0}^{l} S_{ij}(r - r_i)^j, \quad r \in [r_i, r_{i+1}], \quad i = 1, \ldots, n \tag{52}$$

If fixing the (l+1)n free coefficients S_{ij}, the entire spline is determined. It is assumed that $f(r)$ is equal to zero outside [a, b]. Letting the first, second to l-1 order derivatives go to zero at point a, the left boundary conditions (l conditions) are as follows,

$$\begin{pmatrix} S_{10} \\ S_{11} \\ S_{12} \\ \vdots \\ S_{1(l-1)} \end{pmatrix}_{l\times 1} = \begin{pmatrix} 0 \\ 0 \\ 0 \\ \vdots \\ 0 \end{pmatrix}_{l\times 1} \tag{53}$$

The right boundary conditions (l conditions) are

$$\begin{pmatrix} 1 & x_{n+1}-x_n & \left(x_{n+1}-x_n\right)^2 & \left(x_{n+1}-x_n\right)^3 & \cdots & \left(x_{n+1}-x_n\right)^l \\ 0 & 1 & 2\left(x_{n+1}-x_n\right) & 3\left(x_{n+1}-x_n\right)^2 & \cdots & l\left(x_{n+1}-x_n\right)^{l-1} \\ 0 & 0 & 2 & 6\left(x_{n+1}-x_n\right) & \cdots & l\,(l-1)\left(x_{n+1}-x_n\right)^{l-2} \\ \vdots & \vdots & \vdots & \vdots & \ddots & \vdots \\ 0 & 0 & 0 & 0 & \cdots & l!\left(x_{n+1}-x_n\right) \end{pmatrix}_{l\times(l+1)} \begin{pmatrix} S_{n0} \\ S_{n1} \\ S_{n2} \\ S_{n3} \\ \vdots \\ S_{nl} \end{pmatrix}_{(l+1)\times 1} = \begin{pmatrix} 0 \\ 0 \\ 0 \\ 0 \\ \vdots \\ 0 \end{pmatrix}_{l\times 1} \tag{54}$$

Another $l(n-1)$ conditions for the continuity of $S_i(r)$, the first, second to l-order derivatives are as follows

$$\begin{pmatrix} 1 & x_{i+1}-x_i & \left(x_{i+1}-x_i\right)^2 & \cdots & \left(x_{i+1}-x_i\right)^l & -1 & 0 & \cdots & 0 \\ 0 & 1 & 2\left(x_{i+1}-x_i\right) & \cdots & l\left(x_{i+1}-x_i\right)^{l-1} & 0 & -1 & \cdots & 0 \\ \vdots & \vdots & \vdots & \ddots & \vdots & \vdots & \vdots & \ddots & 0 \\ 0 & 0 & 0 & \cdots & l!\left(x_{i+1}-x_i\right) & 0 & 0 & 0 & -1 \end{pmatrix}_{l\times(2l+1)} \begin{pmatrix} S_{i0} \\ S_{i1} \\ S_{i2} \\ \vdots \\ S_{il} \\ S_{(i+1)0} \\ S_{(i+1)1} \\ \vdots \\ S_{(i+1)(l+1)} \end{pmatrix}_{(2l+1)\times 1} = \begin{pmatrix} 0 \\ 0 \\ \vdots \\ 0 \end{pmatrix}_{l\times 1}, \quad i = 1,\ldots,n \tag{55}$$

Eqs.(53)-(55) gives $l+l+l(n-1) = l(n+1)$ conditions. Thus, for calculating (l+1)n unknows, there are still n-l additional conditions to provide. The n-l known moments can provide the additional condition.

$$\begin{aligned} \int_a^b r^k S^{(l)}(r)\,dr &= \sum_{i=1}^{n}\int_{x_i}^{x_{i+1}} r^k S_i(r)\,dr = \sum_{i=1}^{n}\sum_{j=0}^{l} S_{ij}\int_{x_i}^{x_{i+1}} r^k \left(r-r_i\right)^j dr, \quad k = 0,1\ldots,(n-l-1) \\ &= \sum_{i=1}^{n}\left[X_1 S_{i0} + \left(X_2 - x_i X_1\right)S_{i1} + \left(X_3 - 2x_i X_2 + x_i^2 X_1\right)S_{i2} + \cdots + \sum_{j=0}^{l}\left(-1\right)^j C_l^j x_i^{\,j} X_{l-j}\right] = \mu_k \end{aligned} \tag{56}$$

where $X_j = \dfrac{x_{i+1}^{k+j} - x_i^{k+j}}{k+j}$, and C_l^j (j =0,1, …, l) represents the binomial coefficient. According to Eqs.(53)-(56), (l+1)n×(l+1)n linear system of equations ***XS***=***Y*** is built and (l+1)n coefficients S_{ij} is obtained reconstruct $f(r)$ in Eq.(52). In this study, the number of moments is 6. For linear spline (l = 1), the number intervals n = 7; For quadratic spline (l = 2), n = 8; For cubic spline (l = 3), the number intervals n = 9.

3.2. Normalization and regularization

The problem is that a minimum interval [a, b] should be found. In order to improve stability and accelerate search speed, the normalized moments are introduced as follows

$$\hat{\mu}_k = \frac{\mu_k/\mu_0}{\left(\mu_1/\mu_0\right)^k} \tag{57}$$

where 0th and 1st moments are always normalized to 1, namely $\hat{\mu}_0 = \hat{\mu}_1 = 1$. Thus, Eq. (2) is transformed to normalized form, as follows

$$\hat{\mu}_k = \int_0^\infty \hat{r}^k \hat{f}\left(\hat{r}\right) d\hat{r} = \sum_{i=1}^{m} \hat{r}_i^k \hat{w}_i,\ k = 0,1,2,\dots. \tag{58}$$

where $\hat{r}_i$ is normalized radius (abscissa), = r/r_{10} and $\hat{w}_i$ is normalized weight, = w/μ_0. $\hat{f}\left(\hat{r}\right)$ is PDF of normalized radius which is equal to $f(r)/r_{10}$. $f(r)$ is probability density function of radius, namely $f(r)$= $F(r)/\mu_0$, m^{-1}. Thus, $\hat{f}\left(\hat{r}\right)$ is equal to $F(r)\mu_1/\mu_0^2$. Because the mean radius has been normalized to 1, the initial value of solution interval can be set as a =1-ξ_1 and b = 1+ξ_2. If $\int_{\hat{r}_1}^{\hat{r}_2} S_1\left(\hat{r}\right) d\hat{r} < 0.01 f_{\max}\left(\hat{r}_2 - \hat{r}_1\right)$, set a^{k+1}=a^k+0.01(1-a^k) for next iteration step. If $\int_{\hat{r}_n}^{\hat{r}_{n+1}} S_n\left(\hat{r}\right) d\hat{r} < 0.01 f_{\max}\left(\hat{r}_{n+1} - \hat{r}_n\right)$, set b^{k+1} =b^k -0.01(1-b^k) for next iteration step. The truncated singular value decomposition (TSVD) method was used to deal with regularization of ill-posed problem where the small singular values (<1e-5) will be truncated. $\boldsymbol{X}$=$\boldsymbol{U\Lambda V^T}$, Both $\boldsymbol{U}$ and $\boldsymbol{V}$ are orthonormal matrices. $\boldsymbol{\Lambda}$ is a diagonal matrix with singular values of $\boldsymbol{X}$, where λ_1, λ_2, . . ., λ_j are positive.

Besides, when coefficient of deviation C_V is larger than 0.5, the solution has a nonphysical negative radius. To avoid this problem, the constraint of first order derivative of left boundary condition is clear. The new $(l+1)n-1\times(l+1)n$ linear system of equations $\boldsymbol{X_1S}$=$\boldsymbol{Y}$ is under-determined and can also be solved by TSVD method. The pseudo-inverse solution is $\boldsymbol{S}$ =$\boldsymbol{V\Lambda^+U^T}Y$, where $\boldsymbol{\Lambda^+}$ is the Moore-Penrose generalized inverse of $\boldsymbol{\Lambda}$ [55].

4. **Model validation**

4.1. Numerical scheme and boundary conditions

The density-based implicit solver with Roe-FDS convective flux type was utilized to calculate wet steam flow [66]-[67]. The second-order upwind scheme was employed for gas phase and droplet moments of liquid phase. For calculating viscous dissipation and heat conduction accurately, the transition SST turbulent model was used for solving the turbulence k and ω. The two-dimensional structured quad-map grids in whole computational domains were produced. The boundary layer was refined with wall yplus y+ near 1. A pressure inlet boundary with specific total temperature and total pressure, and a pressure outlet with specific backflow temperature and pressure were used. The turbulent intensity Tu at inlet and outlet boundaries were set to be 5% as the medium turbulent intensity. A no-slip adiabatic wall condition was employed. The default value of wall roughness is zero which gives the smooth surface condition.

For experimental validation, Table 1 shows the inlet and outlet boundary conditions of Moore nozzle B and Bakhtar turbine blade. For Moore nozzle B [56], p_{in}^* = 25 kPa and T_{in}^* = 357.6 K. For Bakhtar turbine blade [57], p_{in}^* = 172 kPa and T_{in}^* = 380.66 K. The outflow pressure p_{out} is 0.48p_{in}^*.

The radius spectrum of the submicron droplet is rather difficult to measure. Moore et al. and Bakhtar et al. only measured Sauter radius r_{32} at the outlets of nozzle and blade which has been widely used in the validations of various simulation studies. Thus, the values of Sauter radius r_{32} of CFD is compared with the experimental Sauter radius for the purpose of validation of CFD model.

Table 1 Boundary conditions of Moore nozzle B and Bakhtar turbine blade.

4.2. Experimental validation

In the case of wet steam flow in Moore nozzle B, CFD results of pressure distribution and droplet size by using polydispersed and monodispersed models are compared with experimental data of Moore [56]. The geometry and grid of Moore nozzle B with throat diameter d of 100 mm are illustrated in Fig. 2 and Table 2. The refined mesh where grid number is 450×110 can achieve the grid-independent solution.

Fig. 2 Computational domain and meh refinement of Moore nozzle B.

Table 2 Geometry of Moore nozzle B.

As shown in Fig. 3, the droplet Sauter radius r_{32} in polydispersed model with QMOM approach is smaller than that of Mono one. In CFD, r_{32} = 0.0492 μm at x =370 mm for QMOM while r_{32} = 0.0645 μm for Mono method. Experimental Sauter radius r_{32} = 0.05 μm by spectral turbidity instrument. The relative errors of two models are -1.6% and 29%. It means Sauter radius r_{32} of droplets in polydispersed model is closer to the experimental data. The static pressure distribution at the axis of Moore nozzle B for QMOM and monodispersed models are also compared with experiments. The legend 'dry flow' denotes superheated steam flow without condensation. The computational pressure profiles at nozzle axis demonstrated a good agreement with the experimental data.

Fig. 4 shows nucleation rate, droplet number density and wetness fraction of polydispersed model in comparison with monodispersed model. the nucleation rate and droplet number density of polydispersed model are greater than monodispersed one. Besides the condensation onset and wetness of polydispersed model have a little delay and pressure jump gradient in vicinity of condensation pseudo-shock is larger than that of monodispersed model. The values of Wilson point (the time derivative of the subcooling ΔT_W is 0 and the nucleation rate I reaches the maximum) for polydispersed and monodispersed models are x_w = 75.32 mm and 66.12 mm respectively. The theoretical Wilson point x_w predicted by algebraic formula of Ref [58] is x_w = 78.4 mm, and the experimental value is near to 75 mm. These results indicated the polydispersed model has a better prediction accuracy for Sauter radius.

Fig. 3 Comparison of static pressure and droplet radius of polydispersed and monodispersed models with experiments at the axis of Moore nozzle B.

Fig. 4 Predictions of nucleation rate, droplet number density and wetness of polydispersed and monodispersed models along the nozzle centerline.

The experimental data of Bakhtar [57] was also utilized to validate the polydispersed model. Table 3 given the details of Bakhtar turbine blade. The outlet angle of mid passage φ_{out} = 22.8°. The nominal throat diameter of passage is equal to 4.914 mm. The grid in near wall zone were refined (y plus $\approx$ 1) for predicting velocity profile and entropy generation and entropy transfer very well. By conducting a grid-independent test, the grid 290 × 120 was determined as shown in Fig. 5.

Table 3 Geometry of Bakhtar turbine blade.

Fig. 5 The geometry size and grid of Bakhtar turbine blade.

Fig. 6 illustrated that the static pressure profiles at pressure side and suction side for polydispersed model, monodispersed model and experimental results. There are two pressure jumps on the suction side, due to the condensation pseudo-shock from heat release at x = 18.5 mm and aerodynamic shock at x = 20.5 mm. It also showed that the condensation process of polydispersed model occurs a little delay compared with the monodispersed model. Fig. 7 demonstrated Sauter radius r_{32} of polydispersed model at the mid passage of turbine blade in comparison with the results of monodispersed model and experiments. It also indicated that the Sauter radius r_{32} in polydispersed model is lower than monodispersed one, and the former is closer to the experimental radius. At midline outlet of passage, the values of mean radius r_{32} are 5.962×10^{-8} m, 8.861×10^{-8} m, and 5.70×10^{-8} m [57] for polydispersed method, monodispersed method and experimental measurement, respectively. The predicted errors relative to the experiment result is 4.6% for polydispersed method and 55.4% for monodispersed method. The result indicates that the polydispersed method has a better prediction accuracy for nonequilibrium condensation in the turbine.

Fig. 6 The static pressure distributions at pressure side and suction side of polydispersed model in comparison with monodispersed model and experimental data.

Fig. 7 The Sauter radius r_{32} of polydispersed model in comparison with monodispersed model and experiments along the mid passage of turbine blade.

5. **Nozzle flow**

5.1. Normalized moments and droplet spectrum

According to the formulas of the entropy generations and erosion, the droplet size is a crucial parameter in wet steam flow with condensation and evaporation processes. Under the same boundary conditions of Moore nozzle B (p_{in}^* = 25 kPa, p_{out} = 1.0 kPa and T_{in}^* = 357.6 K), the normalized moments and droplet spectrum are going to be discussed firstly.

Fig. 8 demonstrated that the distributions of normalized moments at the nozzle axis, where 0th and 1st moments are always normalized to 1. Based on the profiles of nucleation rate in Fig. 4, it is found the normalized moments are closely related to the nucleation process. The values of normalized moments $\hat{\mu}_2$,

$\hat{\mu}_3$, $\hat{\mu}_4$ and $\hat{\mu}_5$ in the nucleation zone are greater than results of growth zone. The coefficient of variation C_V = $\sqrt{\hat{\mu}_2 - 1}$. The higher the coefficient of variation C_V, the greater the level of dispersion of droplet radius around the mean radius.

Fig. 8 Distributions of normalized moments at the axis of Moore nozzle B.

As shown in Fig. 8, the dispersion of droplet size in nucleation zone is greater than values of growth zone. The maximums of $\hat{\mu}_2$, $\hat{\mu}_3$, $\hat{\mu}_4$ and $\hat{\mu}_5$ are 1.649, 3.977, 13.119 and 54.985 at x = 63.55 mm, 42.55 mm, 40.18 mm and 39.00 mm, respectively. The peak positions and curve paths of these normalized moments are not same as each other. It indicates that the shape of droplet size distribution $f(r)$ or probability density function will vary along a streamline. Besides, the normalized moments $\hat{\mu}_2$, $\hat{\mu}_3$, $\hat{\mu}_4$ and $\hat{\mu}_5$ tend to be constant values near the nozzle outlet, due to lower subcooling degree and droplet growth rate.

Table 4 presents computed values of 6 moments, number-average radius r_{10} and coefficient of variation C_V from Point A to Point O along the nozzle axis. The number of droplets per unit mass of mixture μ_0 increases up to 8.87×10^{16} kg^{-1} from 5.57×10^{12} kg^{-1}. And in the meantime, the mean radius r_{10} is from 1.28×10^{-9} m to 4.70×10^{-8} m. The coefficient of variation C_V increases first, and then decreases along the streamline.

Table 4 Six moments and number-average radius at different locations along the axis of Moore nozzle B.

By using six moments, quadrature weights w_i and abscissa r_i of QMOM for closure requirement is calculated by PD algorithm. The moments' values at point L in Table 4 are selected as an example. Firstly, the moments are normalized by Eq. (57). Then, the symmetric tridiagonal matrix (Eq. (7)) of PD algorithm. Once the Jacobi matrix has been determined, the abscissas and weights can be solved which are related to eigenvalues and eigen vectors. In this case, the values of normalized abscissa are 0.7281969, 1.0923890, 1.5649833 which means the quadrature abscissa of moments are 2.8265331×10^{-8} m, 4.2401628×10^{-8} m and 6.0745614×10^{-8} m where the mean radius r_{10}= 3.88×10^{-8} m. The normalized weights are 0.3565972, 0.4664764 and 0.1769263 whose sum is equal to 1.

The distributions of abscissa r_i and normalized weight $\hat{w}_i$ by PD algorithm for QMOM at the nozzle axis are shown in Fig. 9 and Table 5. It is worth mentioning that the weights of QMOM inside the nucleation zone (x = 20 ~ 100 mm) have a dramatic change because of the complex relationships among these six moments. The normalized moment $\hat{w}_1$ changes from initial 1.0 down to 0.36. All weights of QMOM stay in parallel downstream of nucleation zone. These results can provide the closure conditions for governing equation of moments.

Table 5 Quadrature weights w_i and abscissa r_i calculated by PD algorithm of six normalized moments at point L (200 mm, 0 mm).

Fig. 9 Distributions of abscissa r_i and normalized weight w_i by PD algorithm for QMOM at the axis of Moore nozzle B.

In addition, it is noteworthy that the droplet spectrum also can be reconstructed from six moments by using the spline-based reconstruction algorithm or some priori shape functions. The reconstructed PDF of normalized radius by using spline-based algorithm with six normalized moments at different locations along the nozzle axis (Point B~D, F, H~O) were plotted in Fig. 10. In most cases, the splines are set to be quadratic for preventing overfitting and mitigating the ill-condition of the matrix.

For the normalized moments by Eq. (57), the means of normalized radius at different locations are a constant 1. However, as shown in Fig. 10, the mode values of PDF of normalized radius gradually change along with the flow direction. At point B (40, 0), the mode is 0.427 with maximum probability density of 0.840; at point F (75, 0), the mode is 0.269 with probability density of 0.856; at point I (90, 0), the mode is 0.651 with probability density of 0.891; at point L (200, 0), the mode is 0.912 with probability density of 1.780; at outlet point 0 (500, 0), the mode is 0.933 with probability density of 1.967. It is found that all of mode values of PDF are less than its mean 1. Besides, the confidence interval of PDF also varies widely. It is noteworthy that 95% confidence interval is from [0.12, 2.89] at point B to [0.62, 1.48] at outlet point O.

Fig. 10 Reconstructed PDF of normalized radius by using quadratic spline-based algorithm at different locations along the axis of Moore nozzle B.

Fig. 11 showed comparison of reconstruction of probability density function $f(r)$ of droplet size between splined-based algorithm from six moments and priori shape functions from three moments. At point C in initial nucleation zone, spline reconstruction is closer to gamma distribution as shown in Fig. 11 (a). The mode values of spline distribution and gamma distribution are 1.11×10^{-9} m and 1.35×10^{-9} m, while the mode values of Gauss and log-normal distribution are 1.69×10^{-9} m and 3.55×10^{-9} m. it should be noticed that, because the deviation coefficient C_V is 0.779, the radius of Gauss distribution appears unphysical negative value. The shape of probability density function $f(r)$ of droplet size at point I in Fig. 11 (b) is similar to point C in Fig. 11 (a). It revealed that the actual probability distribution in the nucleation zone is closer to a gamma distribution.

Fig. 11 Reconstruction of probability density function $f(r)$ by using splined-based algorithm and priori shape functions from several moments at different locations along the axis of Moore nozzle B.

As the droplets enter into the growth zone, the shape of droplet number density function will change gradually. The reconstructions of probability density function $f(r)$ by using spline-based algorithm at point L and point O were plotted in Fig. 11 (c)-(d). The results showed the spline distribution in growth zone is closer to the log-normal distribution.

5.2. Droplet evaporation with aerodynamic shock

The evaporation of droplets occurs in the nozzle and turbine when the droplets enter superheated region or pass through an aerodynamic shock wave. Next, different back pressure ratio values were specified to examine the effect of shock wave on QMOM model performance for predicting droplet spectrum. Fig. 12 illustrated the profiles of static pressure along the nozzle centerline with subsonic and supersonic outflows for dry cases and polydispersed wet cases. The corresponding Sauter radius and wetness fraction of polydispersed model for wet cases were shown in Fig. 13.

Fig. 12 Distribution of pressure ratio of polydispersed model with QMOM approach at the axis of Moore nozzle B with subsonic and supersonic outflows for dry and wet cases.

Fig. 13 The distributions of Sauter radius and wetness fraction of polydispersed model with QMOM approach at the axis of Moore nozzle B for various back pressures.

In the case of supersonic outflow, there are no aerodynamic shock waves in the flow field. The pressure jump is the condensation pseudo-shock occurring at point x = 75.32 mm (Wilson point) with the maximum supercooling degree of 35.05 K, where, the pressure increases from 0.37 to 0.43. After the peak nucleation, the supercooling degree drops drown to 2 K quickly shown in Fig. 13. It also showed there is a sharp rise of wetness fraction near the shock pseudo-shock and then wetness fraction increases continuously along the flow direction. In the case of subsonic outflow with aerodynamic shock, the outlet back pressures were specified as p_{out} = 12 kPa, 14 kPa, and 16 kPa. As shown in Fig. 12, with the increase of the back pressure, the aerodynamic shock moves toward the nozzle throat. It also is found that the shock location of wet case is lag behind dry case when the other conditions are the same. After the aerodynamic shock, the supercooling degree suddenly becomes negative and the vapor is superheated, as shown in Fig. 13. Thus, the droplets will rapidly evaporate in superheated conditions.

In addition, downstream of the aerodynamic shock, a cap-shock pattern with a slight dip of pressure is observed which is consistent with the experiment of Papamoschou [59]. The shock compression pressure jump is followed by a rapid expansion wave and then the pressure drops down to the small plateau. Actually, this phenomenon can be explained by shock structure. Fig. 14 showed the contours of Mach number and shock separation in the nozzle when p_{out} = 14 kPa (subsonic outflow). The asymmetric lambda shock and separated flow in a symmetric nozzle was obtained. Lambda shape consists the incident shock C1, reflected shock C2, the triple point T1 and Mach stem [60]. There are two different shock induced separation types can exist in the nozzle, namely free shock separation (FSS) and restricted shock separation (RSS). The lambda shock and separation significantly affect the level of evaporation and wetness fraction.

Fig. 14 Contours of Mach number and shock separation in Moore nozzle B: compared dry case (a) and wet case (b) when p_{out} = 14 kPa (subsonic outflow).

Fig. 15 shows the contours of wetness fraction in the nozzle for various back pressures. It is noticed that the spatial distributions of wetness fraction are also asymmetry when p_{out} = 12 kPa, 14 kPa, and 16 kPa. The maximum values of wetness fraction are 0.0401 at point (420, -35), 0.0355 at point (345, -22), 0.0315 at point (285, -15), respectively. The spatial distributions of wetness fraction in the case of subsonic outflow is more complex. Thus, the performance of QMOM model for predicting droplet evaporation with lambda shock should also be checked.

Fig. 15 Contours of wetness fraction in Moore nozzle B for various back pressures.

The reconstructions of probability density function $f(r)$ of droplet size at nozzle outlet point O (500, 0) for various back pressure values were plotted in Fig. 16. As mentioned, reconstructed spline shape at outlet with supersonic outflow is closer to the log-normal distribution. However, the reconstructed shape changes into an approximate gamma distribution affected by the evaporation when the back pressures are 12 kPa and 16 kPa.

Fig. 16 Reconstructed $f(r)$ by splined-based algorithm and priori function shapes at nozzle outlet point O (500, 0) for various back pressure values.

6. **Blade cascade flow**

6.1. Wetness distributions and Droplet spectrum

The proposed polydispersed model with QMOM approach will be utilized to analyze the droplet spectrum, exergy destruction and erosion rate in a linear turbine blade. Firstly, the contours of Mach number, mass change rate and wetness fraction of polydispersed model were plotted in Fig. 17-Fig. 19. $p_{in}^* = 172$ kPa and $T_{in}^* = 380.66$ K. The subcooling degree of inlet is 8 K, thus the Wilson point is at the subsonic region and condensation pseudo-shock does not appear in nucleation region.

As shown in Fig. 17 (a), a weak oblique shock wave which remains supersonic behind the shock wave is observed near the trailing edge when back pressure $p_{out}/p_{in}^* = 0.30$. The pressure side shock wave S_P occurs at Ma =1.43 and suction side shock wave S_S appears at Ma =1.50. In Fig. 17 (b) and (c), it showed an evaporation zone (mass change rate m_v is -1850 kg m^{-3} s^{-1}) and a secondary condensation zone appear downstream of oblique shock. Thus, there are 4 circular isolines along the blade passage as shown in Fig. 17 (a). Besides, it also illustrated that the wake and flow deviation angle will be affected by interaction of a reflected shock with the boundary layer.

Fig. 17 The contours of Mach number, mass change rate and wetness fraction of polydispersed model with QMOM approach in turbine blade for back pressure ratio p_{out}/p_{in}^* =0.30.

Fig. 18 shows the computed results of back pressure $p_{out}/p_{in}^* = 0.50$. The maximum Mach number is reduced to 1.08. As shown in Fig. 18 (a), a strong oblique shock wave which is subsonic behind the shock wave is observed near the trailing edge. After the shock, secondary condensation shown in Fig. 18 (b) will increase the flow velocity and then recover the supersonic flow at the outlet. Fig. 18 (c) shows the wetness fraction β at the outlet is reduced to 0.038. In addition, the wetness fraction β in the wake region is smaller than other regions.

Fig. 18 The contours of Mach number, mass change rate and wetness fraction of polydispersed model with QMOM approach in turbine blade for back pressure ratio p_{out}/p_{in}^* =0.50.

When the back pressure is p_{out}/p_{in}^* = 0.50, the entire flow field is subsonic as shown in Fig. 19 (a). The shock wave disappears at the trailing edge. The evaporation is quite weak where the maximum evaporation rate is only 500 kg m^{-3} s^{-1} in Fig. 19 (b). As shown in Fig. 19 (c), the wetness fraction is basically a constant of 0.024 because the weak evaporation and secondary condensation can be ignored.

Fig. 19 The contours of Mach number, mass change rate and wetness fraction of polydispersed model with QMOM approach in turbine blade for back pressure ratio p_{out}/p_{in}^* =0.70.

Next, the results of reconstructed probability density function *f*(*r*) of droplet size by using splined-based algorithm in turbine blade were also plotted and discussed. The comparisons of the reconstructed *f*(*r*) between splined-based algorithm and priori function shapes at point A (20, 44), point B (21,42) and point C (30 20) of turbine blade when p_{out}/p_{in}^* =0.30 and 0.50 were shown in Fig. 20 (a) and (b). Taking the point B for an example, the mean radius r_{10} is 3.64×10^{-8} m and Sauter radius r_{32} is 4.59×10^{-8} m. The mode of spline-based probability density function is 3.20×10^{-8} m with probability density of 3.21×10^{7} m^{-1}, while the mode of gamma distribution is 3.13×10^{-8} m with probability density of 3.18×10^{7} m^{-1}. The results revealed that reconstructed splines are closer to gamma distribution in turbine blade everywhere.

Fig. 20 Reconstructed *f*(*r*) by splined-based algorithm and priori function shapes from several moments in turbine blade.

6.2. Exergy destruction and erosion rate

Finally, exergy destruction, Baumann factor and erosion rate of turbine blade were calculated by polydispersed and monodispersed models. According to Eqs. (30)-(36), the multi-component entropy generations of wet steam flow of polydispersed model in turbine blade are were in Fig. 21 and Table 6. The value of wall roughness is 0 for smooth blade and 0.1mm for rough blade. As mentioned, the entropy generation $s_{gen,D}$ is viscous losses in boundary layer and wake. $s_{gen,C}$ is dependent on heat transfer of boundary layer. $s_{gen,L}$ attributes to condensation and evaporation. $s_{gen,A}$ derives from aerodynamic shock and loss in the multi-dimensional non-isentropic flow.

Fig. 21 showed the predictions of QMOM for multi-component entropy generations of smooth and rough blade operating at different back pressure values. It is quite obvious that $s_{gen,L}$ and $s_{gen,A}$ are the most dominant sources of exergy destruction. In smooth blade, the entropy generation of phase change $s_{gen,L}$ increases from 5.886 to 19.775 J kg^{-1} K^{-1} when back pressure p_{out}/p_{in}^* is range from 0.30 to 0.70. It revealed the roughness will affect the boundary layer transition, turbulence viscosity and turbulence thermal diffusivity. When p_{out}/p_{in}^* = 0.50, $s_{gen,A}$ and $s_{gen,D}$ are 21.151 and 6.025 in smooth blade, while corresponding values increase to 24.704 and 15.006 J kg^{-1} K^{-1} in rough blade.

As shown in Fig. 21, the percentages of four types of entropy generations in wet flow can also be calculated. Due to the roughness effect, the percentage of $s_{gen,D}$ increases from 11.32% to 22.75%, and the percentage of $s_{gen,C}$ rises from 0.35% to 5.91% for $p_{\mathrm{out}}/p_{\mathrm{in}}^* = 0.30$.

Table 6 presented the data of the entropy generations of dry flow, to assess the effect of phase change. It is found that entropy generation s_{gen} in smooth blade for $p_{\mathrm{out}}/p_{\mathrm{in}}^* = 0.30$ gradually grows from 16.428 for dry flow to 64.638 J kg^{-1} K^{-1} for wet flow. Besides, a comparison of the entropy generation between the polydispersed model and monodispersed model was shown in Table 6. Generally total entropy generation s_{gen} in the QMOM method is 8% larger than Mono method.

Fig. 21 Radar charts of multi-component entropy generations of wet steam flow of the polydispersed model with smooth and rough walls at different back pressures.

According to Eq. (38), the values of specific exergy destruction e_D at various condition were obtained. As shown in Table 6, The maximum exergy destruction e_D is equal to 25.293 kJ kg^{-1}. For LP steam turbines with $q_{\mathrm{m}} = 144.5$ kg s^{-1} [12], the maximum exergy destruction rate E_D (kW) is 3.65 MW.

Table 6 Mass-weighted average of entropy generations (J·kg^{-1}·K^{-1}) of blade outlet for the polydispersed, monodispersed and dry models at various back pressure ratio $p_{\mathrm{out}}/p_{\mathrm{in}}^*$.

For $p_{\mathrm{in}}^* = 172$ kPa and $T_{\mathrm{in}}^* = 380.66$ K, inlet specific flow exergy $e_{x,\mathrm{in}}$ is equal to 568.4 kJ·kg^{-1}. The exergy destruction ratio ζ_D calculated by Eq. (40) were shown in Fig. 22 (a). The back pressure, phase change and wall roughness will affect the exergy destruction ratio ζ_D. As observed in figure, the QMOM rough case has a highest exergy destruction ratio, followed by QMOM smooth case, Mono case and dry case. The exergy destruction ratio increases with decreasing of back pressure. In the QMOM smooth case, ζ_D grows from 1.04% to 3.39% for five back pressures. If the wall condition is roughness, the value grow up to a maximum of 4.45% for $p_{\mathrm{out}}/p_{\mathrm{in}}^* = 0.30$.

Fig. 22 The mass-weighted averages of exergy destruction ratio, Baumann factor and normalized erosion rate for wet and dry cases at different back pressure and wall roughness values.

According to Fig. 22 (a) and Eq. (41), the Baumann factor a_B for wetness loss correlation was calculated as shown in Fig. 22 (b). A considerable range of a_B (0.4~2.5) was observed experimentally based on a significant amount of turbine tests [12]. In this study, the range of Baumann factor a_B is 0.574~1.312. In the smooth blade, the average of Baumann factor a_B is 0.728 for QMOM and 0.644 for Mono method. It indicated that the predicted Baumann factor for wetness loss have a good agreement with empirical levels.

In addition, normalized erosion rate depending on droplet size and wetness fraction were shown in Fig. 22 (c). It demonstrated that erosion rate of polydispersed model is only 58.4%~64.4% of monodispersed model. The reason is Sauter radius predicted by monodispersed model is higher than the truth value, as shown in Fig. 7. It revealed that proposed polydispersed model with QMOM approach is better for predicting the droplet spectrum, energy loss and erosion rate in wet steam turbine.

7. **Conclusion**

This paper proposed a polydispersed model with QMOM approach combining the transition SST model and entropy transport equation to investigate the droplet spectrum, wetness fraction, entropy generation, exergy destruction ratio and erosion rate of nonequilibrium flow in the turbine. The droplet spectrum was reconstructed by using spline-based algorithm from a finite number of moments without prior knowledge. It showed the static pressure and Sauter radius predicted by polydispersed model agreed well with the experimental results. The moments distributions and droplet spectra of wet steam flow in the nozzle and turbine were analyzed. The exergy destruction and erosion rate were also obtained.

(1) For the nozzle flow, it is concluded that,

a) The droplet spectrum shape is changeable and the span is broader. The variation coefficient C_V of PDF increases first, and then decreases along the streamline ranging of 0.212~0.794. The mode value of PDF of normalized radius ranges from 0.269 to 0.933, all of whose mean is one.
b) For supersonic outflow, the shape of droplet spectrum is closer to gamma distribution in nucleation zone and log-normal distribution in growth zone.
c) For the subsonic outflow, the shapes are more like a gamma distribution in the whole flow field, due to effect of asymmetric lambda shock and droplet evaporation.

(2) For the blade cascade flow, it is concluded that:

a) There is a weak oblique shock wave near the trailing edge when $p_{\mathrm{out}}/p_{\mathrm{in}}^* = 0.30$ while a strong oblique shock when $p_{\mathrm{out}}/p_{\mathrm{in}}^* = 0.50$. The oblique shock induces a complex droplet evaporation and secondary condensation, leading to reconstructed shape is closer to gamma distribution in turbine.
b) The entropy generation of phase change is 5.886 ~ 19.775 J kg^{-1} K^{-1} in smooth blade. Due to the roughness effect, the percentage of entropy generation of viscous loss increases from 11.32% to 22.75% and heat conduction loss rises from 0.35% to 5.91% for $p_{\mathrm{out}}/p_{\mathrm{in}}^* = 0.30$.
c) The maximum exergy destruction is equal to 25.293 kJ·kg^{-1}. QMOM rough case has a highest exergy destruction ratio, followed by QMOM smooth case, Mono case and dry case.
d) The exergy destruction ratio increases from 1.04% to 4.45%. The range of Baumann factor is 0.574~1.312. In smooth blade, the average of Baumann factor a_B is 0.728 for QMOM. Besides, the erosion rate in the polydispersed model is only 58.4%~64.3% of monodispersed model.

This study provides a useful technique to evaluate droplet spectrum and energy loss of the turbine equipment and help the shape optimization of turbine blade.

Acknowledgement

This work is supported in part by National Natural Science Foundation of China under Grant 51876143, 61873184, and 61627803, in part by European Union’s Horizon 2020 research and innovation programme under the Marie Sklodowska-Curie grant agreement No 792876.

References

[1]. Xu J, Gu Y, Ma S. Data based online operational performance optimization with varying work conditions for steam-turbine system. Appl. Therm. Eng. 2019; 151: 344-353.

[2]. Aliabadi M, Lakzian E, Khazaei I, et al. A comprehensive investigation of finding the best location for hot steam injection into the wet steam turbine blade cascade. Energy 2020;190: 116397.

[3]. Starzmann J, Casey MM, Mayer JF and Sieverding F. Wetness loss prediction for a low pressure steam turbine using computational fluid dynamics, Proc. Inst. Mech. Eng. Part A: J. Power Energy 2014;228(2):216-231.
[4]. Haseli Y. Efficiency improvement of thermal power plants through specific entropy generation. Energ. Convers. Manage. 2018; 159:109-20.
[5]. Wang C, Wang L, Zou T and Zhang H. Influences of area ratio and surface roughness on homogeneous condensation in ejector primary nozzle. Energ. Convers. Manag. 2017; 149:168-174.
[6]. Gavrilov I, Popov V, Sorokin I, et al. A contactless technique for determining the average sizes of erosion-hazardous droplets in polydisperse wet steam flow. Therm. Eng. 2014; 61(8): 577-584.
[7]. Aliabadi M, Lakzian E, Jahangiri A, et al. Numerical investigation of effects polydispersed droplets on the erosion rate and condensation loss in the wet steam flow in the turbine blade cascade. Appl. Therm. Eng. 2020; 164: 114478.
[8]. Wang C, Wang X, Ding H. Boundary layer of non-equilibrium condensing steam flow in a supersonic nozzle. Appl. Therm. Eng. 2018; 129: 389-402.
[9]. Ding H, Wang C, Chen C. Non-equilibrium condensation of water vapor in sonic nozzle. Appl. Therm. Eng. 2014; 71(1): 324-334.
[10]. Mohammed MK, Al Doori WH, Jassim AH, Ibrahim TK, Al-Sammarraie AT. Energy and exergy analysis of the steam power plant based on effect the numbers of feed water heater. J. Adv. Res. Fluid Mech. Therm. Sc 2019; 56:211-222.
[11]. Hughes FR, Starzmann J, White AJ, et al. A comparison of modeling techniques for polydispersed droplet spectra in steam turbines. J. Eng. Gas Turb. Power 2016; 138(4).
[12]. Petr V, Kolovratnik M. Modelling of the droplet size distribution in a low-pressure steam turbine. Proc. Inst. Mech. Eng., Part A: J. Power Energy 2000; 214(2): 145-152.
[13]. Tatsuno K, Nagao S. Water droplet size measurements in an experimental steam turbine using an optical fiber droplet sizer. J. Heat Transf. 1986;108(4):939-945.
[14]. Ahmad M, Schatz M, Casey M V. Experimental investigation of droplet size influence on low pressure steam turbine blade erosion. Wear 2013;303(1-2):83-86.
[15]. Wang N, Wei J, Cai X, et al. Optical measurement of wet steam in turbines. J. Eng. Gas Turbines Power 1998;120(4):867-871.
[16]. Tabakoff W, Hamed A, Metwally M. Effect of particle size distribution on particle dynamics and blade erosion in axial flow turbines. J. Eng. Gas Turbines Power 1991;113(4):607-615.
[17]. Alekseev R, Gribin V, Tishchenko A, et al. Application of PTV method for investigation of polydisperse wet steam flow, Journal of Physics: Conference Series. IOP Publishing 2018;1128(1):012093.
[18]. Filippov G, Gribin V, Tischenko A, et al. Experimental studies of polydispersed wet steam flows in a turbine blade cascade. Proc. Inst. Mech. Eng., Part A: J. Power Energy 2014;228(2):168-177.
[19]. Raoult F, Lacour S, Carissimo B, et al. CFD water spray model development and physical parameter study on the evaporative cooling. Appl. Therm. Eng. 2019; 149: 960-974.
[20]. Gerber AG. Two-phase Eulerian/Lagrangian model for nucleating steam flow. J. Fluids Eng. 2002; 124:465-475
[21]. Yamamoto S, Tanuma T. Numerical study of unsteady gas and steam turbine cascade flows, Proceedings of the International Gas Turbine Congress 1999:489-496.

[22]. Dykas S and Wróblewski W. Single-and two-fluid models for steam condensing flow modeling. Int. J. Multiph. Flow 2011;37(9):1245-1253.
[23]. Wróblewski W and Dykas S. Two-fluid model with droplet size distribution for condensing steam flows. Energy 2016; 106:112-120.
[24]. Abadi SNR, Kouhikamali R, Atashkari K. Two-fluid model for simulation of supersonic flow of wet steam within high-pressure nozzles. Int. J. Therm. Sci. 2015; 96:173-182.
[25]. Han X, Zeng W and Han Z. Investigation of the comprehensive performance of turbine stator cascades with heating endwall fences. Energy, 2019;174:1188-1199.
[26]. White AJ, Young JB. Time-marching method for the prediction of two-dimensional, unsteady flows of condensing steam. J. Propul. Power 1993.
[27]. Starzmann J, Schatz M, Casey MV, et al. Modelling and validation of wet steam flow in a low pressure steam turbine. ASME 2011 Turbo Expo: Turbine Technical Conference and Exposition. American Society of Mechanical Engineers Digital Collection 2011: 2335-2346.
[28]. Yang Y, Zhu X, Yan Y, Ding H, Wen C, Performance of supersonic steam ejectors considering the nonequilibrium condensation phenomenon for efficient energy utilization. Appl. Energy 2019; 15(242):157-167.
[29]. Zhang G, Wang L, Zhang S, et al. Effect evaluation of a novel dehumidification structure based on the modified model. Energy Convers. Manage. 2018; 159:65-75.
[30]. Zhang G, Wang F, Wang D, Wu T, Qin X. and Jin Z. Numerical study of the dehumidification structure optimization based on the modified model. Energy Convers. Manage. 2019; 181:159-177.
[31]. Zhang G, Zhang X, Wang D, et al. Performance evaluation and operation optimization of the steam ejector based on modified model. Appl. Therm. Eng. 2019; 163: 114388.
[32]. Edathol J, Brezgin D, Aronson K and Kim HD. Prediction of non-equilibrium homogeneous condensation in supersonic nozzle flows using Eulerian-Eulerian models. Int. J. Heat Mass Transf., 2020;152:119451.
[33]. White AJ, Hounslow MJ. Modelling droplet size distributions in polydispersed wet-steam flows. Int. J. Heat Mass Transf. 2000; 43(11): 1873-1884.
[34]. Wongsarivej P, Tanthapanichakoon W. A model for a non-uniform spray evaporator taking into account the effect of non-isothermal polydisperse droplets. Int. J. Heat Mass Transf. 2015; 90: 1170-1177.
[35]. White AJ. A comparison of modelling methods for polydispersed wet-steam flow. Int. J. Numer. Meth. Eng. 2003; 57(6): 819-834.
[36]. Gerber AG, Kermani MJ. A pressure based Eulerian–Eulerian multi-phase model for non-equilibrium condensation in transonic steam flow. Int. J. Heat Mass Transf. 2004; 47(10-11):2217-2231.
[37]. Gerber AG, Mousavi A. Representing polydispersed droplet behavior in nucleating steam flow. J. Fluids Eng. 2007;129(11):1404-1414.
[38]. Afzalifar A, Turunen-Saaresti T, Grönman A. Comparison of moment-based methods for representing droplet size distributions in supersonic nucleating flows of steam. J. Fluids Eng. 2018;140(2).
[39]. Hulburt HM, Stanley K. Some problems in particle technology: A statistical mechanical formulation. Chem. Eng. Sci. 1964; 19:555-74.

[40]. Diemer R B, Olson J H. A moment methodology for coagulation and breakage problems: Part 2-moment models and distribution reconstruction. Chem. Eng. Sci. 2002;57(12):2211-2228.
[41]. John V, Angelov I, Öncül A, et al. Techniques for the reconstruction of a distribution from a finite number of its moments. Chem. Eng. Sci. 2007;62(11): 2890-2904.
[42]. Souza L, Janiga G, John V, et al. Reconstruction of a distribution from a finite number of moments with an adaptive spline-based algorithm. Chem. Eng. Sci. 2010;65(9):2741-2750.
[43]. Ibrahim TK, Mohammed MK, Awad OI, et al. A comprehensive review on the exergy analysis of combined cycle power plants. Renew. Sust. Energ. Rev. 2018; 90:835-850.
[44]. McGraw R. Description of aerosol dynamics by the quadrature method of moments. Aerosol. Sci. Tech., 1997;27(2):255-65.
[45]. Gordon RG. Error bounds in equilibrium statistical mechanics. J. Math. Phys. 1968;9(5):655-63.
[46]. Ding H, Li Y, Lakzian E, et al. Entropy generation and exergy destruction in condensing steam flow through turbine blade with surface roughness. Energ. Convers. Manage. 2019; 196:1089-104.
[47]. Vargaftik NB, Volkov BN, Voljak LD. International Tables of the Surface Tension of Water. J. Phys. Chem. Ref. Data. 1983;12(3):817-20.
[48]. Moskalenko AB and Kozhevnikov AI. Estimation of gas turbine blades cooling efficiency. Procedia. Eng. 2016;150(1):61-67.
[49]. Kermani MJ, Gerber AG. A general formula for the evaluation of thermodynamic and aerodynamic losses in nucleating steam flow. Int. J. Heat Mass Transf. 2003; 46:3265-3278.
[50]. Moran MJ, Shapiro HN, Boettner D, et al. Fundamentals of engineering thermodynamics. John Wiley and Sons 2010, Dec 7.
[51]. Beer JM. High efficiency electric power generation: The environmental role. Prog. Energ. Combust. 2007; 33:107-134.
[52]. Vučković GD, Stojiljković MM, Vukić, MV. First and second level of exergy destruction splitting in advanced exergy analysis for an existing boiler. Energy Convers. Manage. 2015; 104:8-16.
[53]. Mirhoseini MS, Boroomand M. Multi-objective optimization of hot steam injection variables to control wetness parameters of steam flow within nozzles, Energy 2017; 141:1027-1037.
[54]. Lee BE, Riu KJ, Shin SH, Kwon SB. Development of a water droplet erosion model for large steam turbine blades, KSME Int. J. 2003;17(1):114-121.
[55]. Xu P. Truncated SVD methods for discrete linear ill-posed problems, Geophys. J. Int. 1998;135(2):505-514.
[56]. Moore MJ, Walters PT, Crane RI, et al. Predicting the fog drop size in wet steamturbines, in: Wet Steam 4 Conference, Institute of Mechanical Engineers (UK), University of Warwick, 1973:37-73.
[57]. Bakhtar F, Mahpeykar MR, Abbas K. An investigation of nucleating flows of steam in a cascade of turbine blading-theoretical treatment. J. Fluid Eng. 1995;117(1): 138-144.
[58]. Ding H, Wang C, Wang G. Analytic equations for the Wilson point in high pressure steam flow through a nozzle. Int. J. Heat. Mass. Transf. 2015; 91:961-968.
[59]. Xiao Q, Tsai HM, Papamoschou D. Numerical investigation of supersonic nozzle flow separation. AIAA J 2007;45(3): 532-541.
[60]. Ding H, Wang C, Wang G. Transient conjugate heat transfer in critical flow nozzles. Int. J. Heat Mass Transf. 2017; 104:930-942.
[61]. Wu K, Raman SK, Sethuraman VRP, Zhang G, Kim HD. Effect of the wall temperature on Mach

stem transformation in pseudo-steady shock wave reflections. Int. J. Heat Mass Transf. 2020; 147:118927.
[62]. Young JB. Spontaneous condensation of steam in supersonic nozzles. Physicochem. Hydrodyn. 1982; 3: 57-82.
[63]. Han X, Zeng W, Han Z. Investigating the dehumidification characteristics of the low-pressure stage with blade surface heating. Appl. Therm. Eng. 2020; 164: 114538.
[64]. Yu X, Xie D, Wang C, et al. Numerical Investigation of oscillating flows with nonequilibrium condensation in nozzles. J. Propul. Power 2015; 31(3): 837–842.
[65]. Abadi S, Ahmadpour A, Abadi S, et al. CFD-based shape optimization of steam turbine blade cascade in transonic two phase flows. Appl. Therm. Eng. 2017; 112:1575-1589.
[66]. Roe PL. Characteristic-based schemes for the Euler equations. Annu. Rev. Fluid Mech. 1986 Jan;18(1):337-65.
[67]. Takahashi Y, Chen L, Okajima J, et al. Interferometric measurement and numerical comparisons of supersonic heat transfer flows in microchannel. Appl. Therm. Eng. 2016; 109: 582-590.

List of Figure Captions and Table Titles

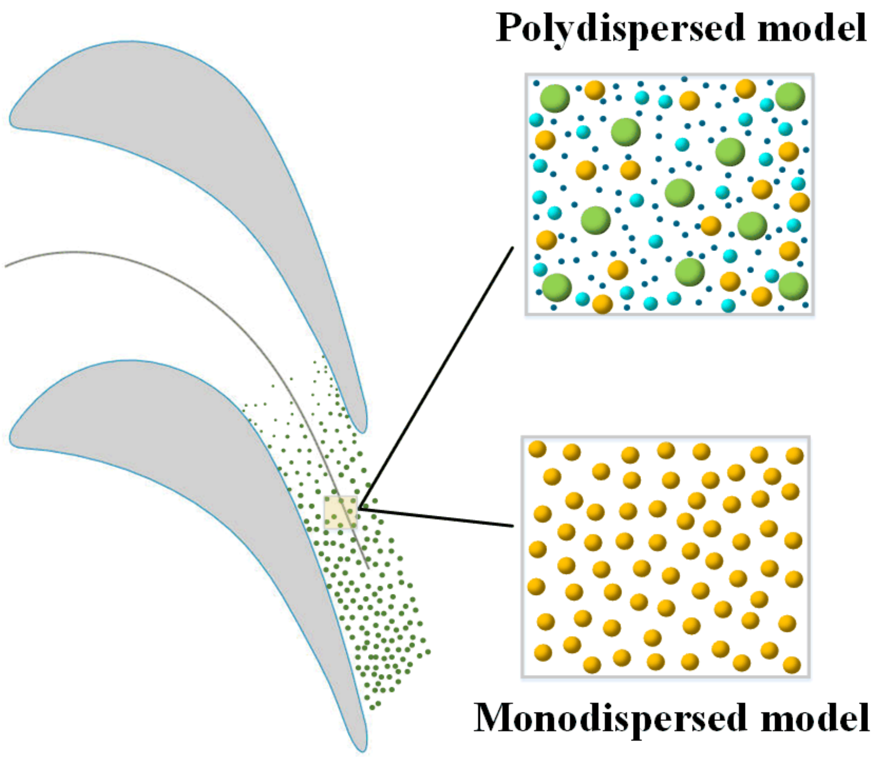

Fig. 23 Polydisperse and monodispersed models for wet steam flows with homogeneous condensation.

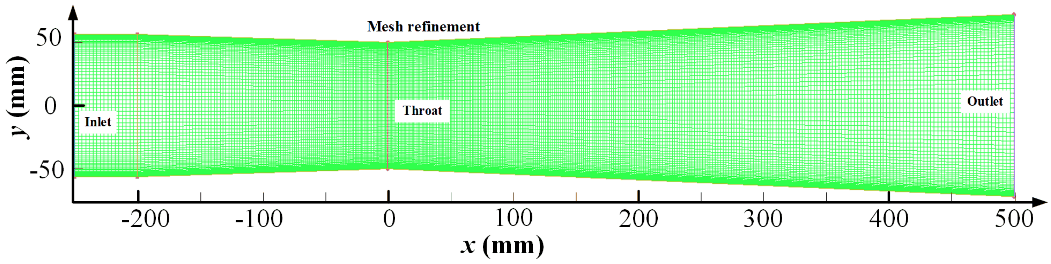

Fig. 24 Computational domain and meh refinement of Moore nozzle B.

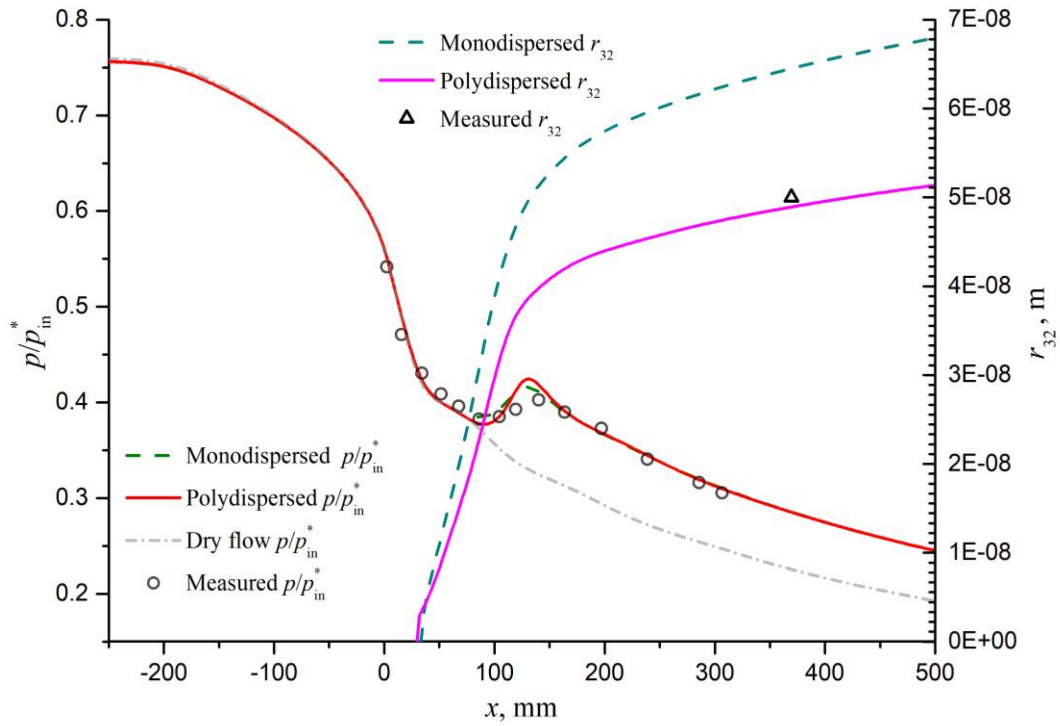

Fig. 25 Comparison of static pressure and droplet radius of polydispersed and monodispersed models with experiments at the axis of Moore nozzle B.

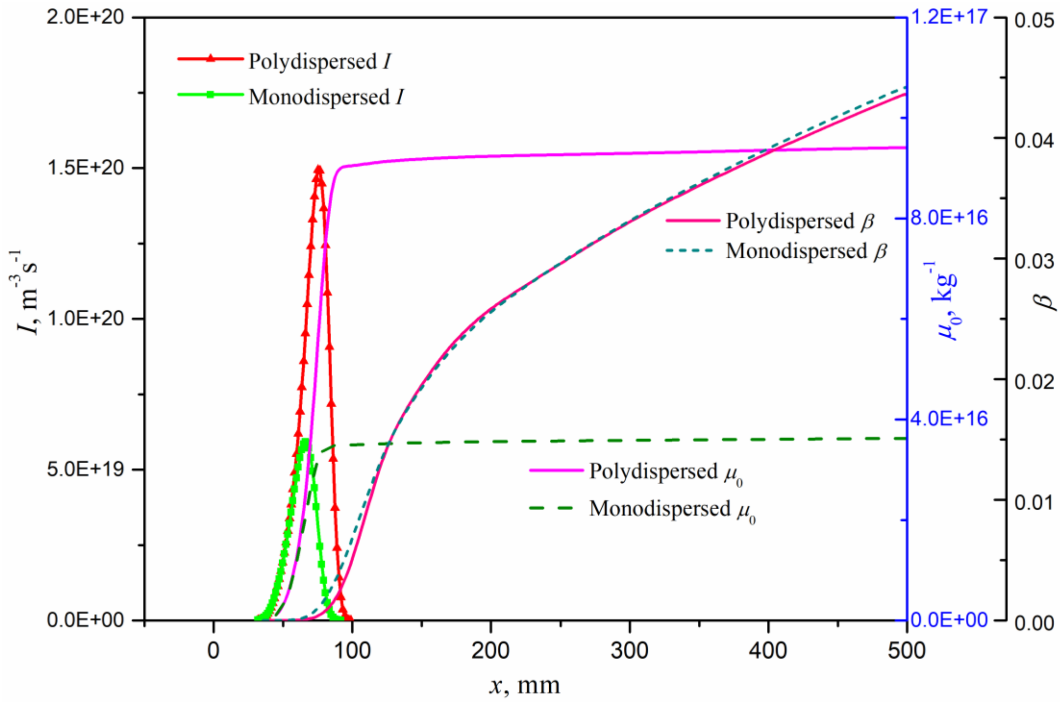

Fig. 26 Predictions of nucleation rate, droplet number density and wetness of polydispersed and monodispersed models along the nozzle centerline.

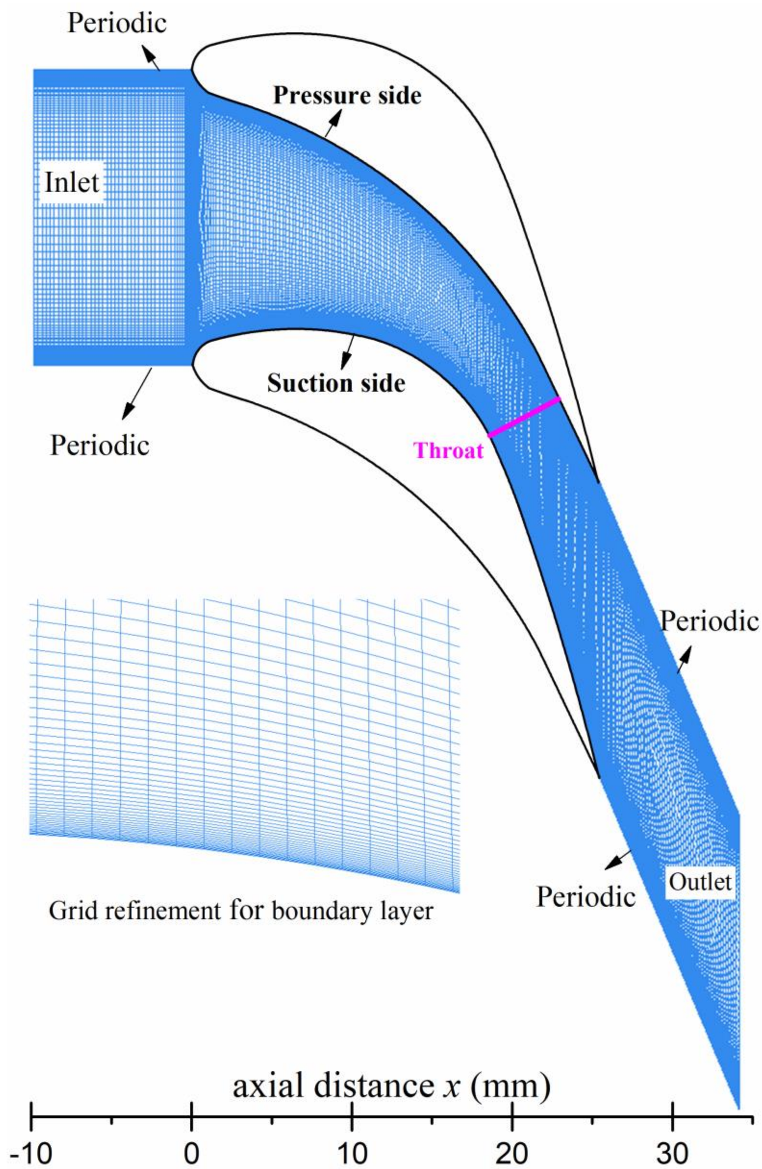

Fig. 27 The geometry size and grid of Bakhtar turbine blade.

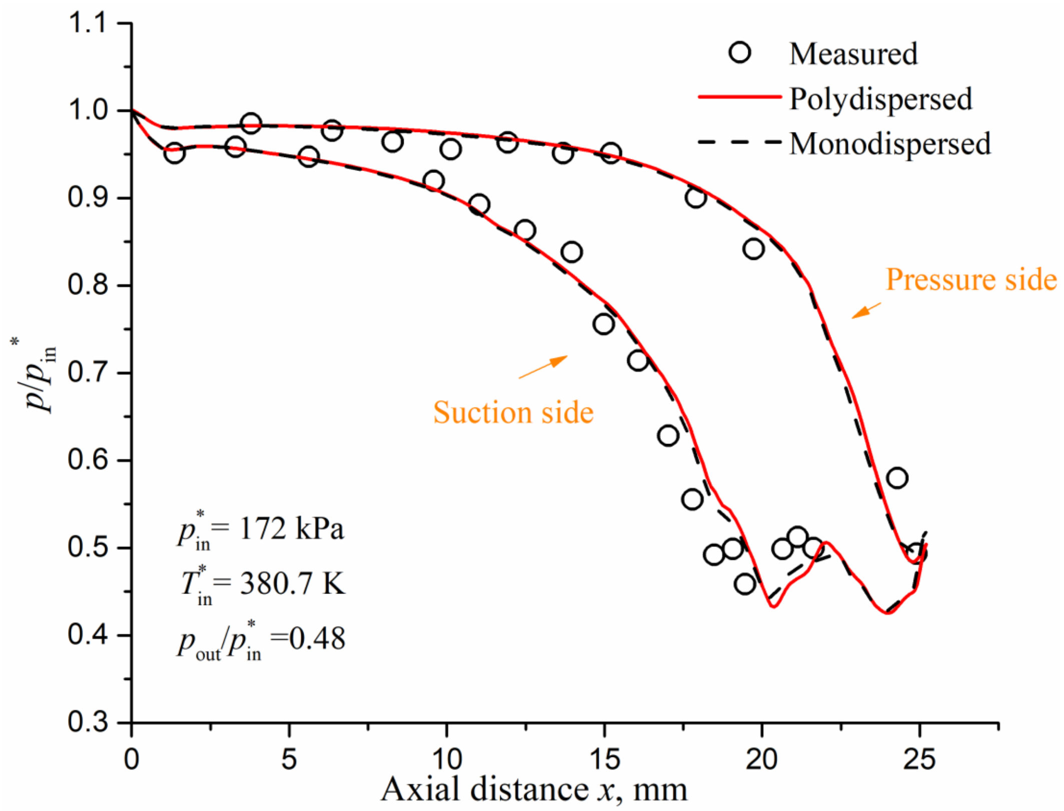

Fig. 28 The static pressure distributions at pressure side and suction side of polydispersed model in comparison with monodispersed model and experimental data.

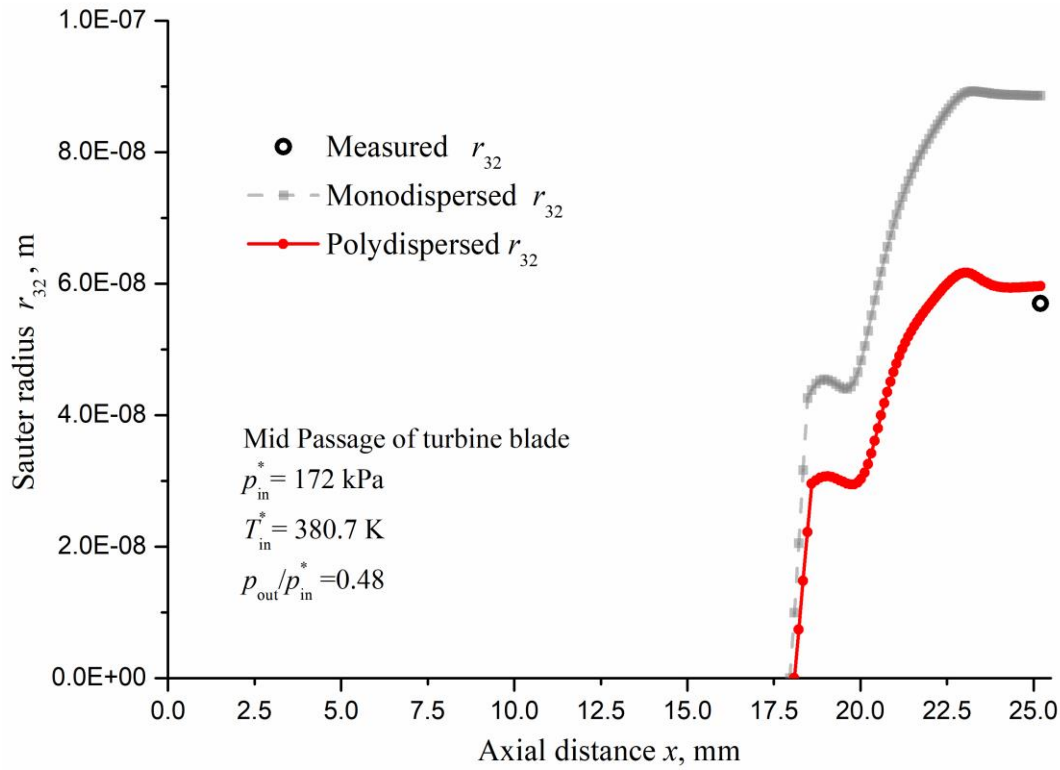

Fig. 29 The Sauter radius r_{32} of polydispersed model in comparison with monodispersed model and experiments along the mid passage of turbine blade.

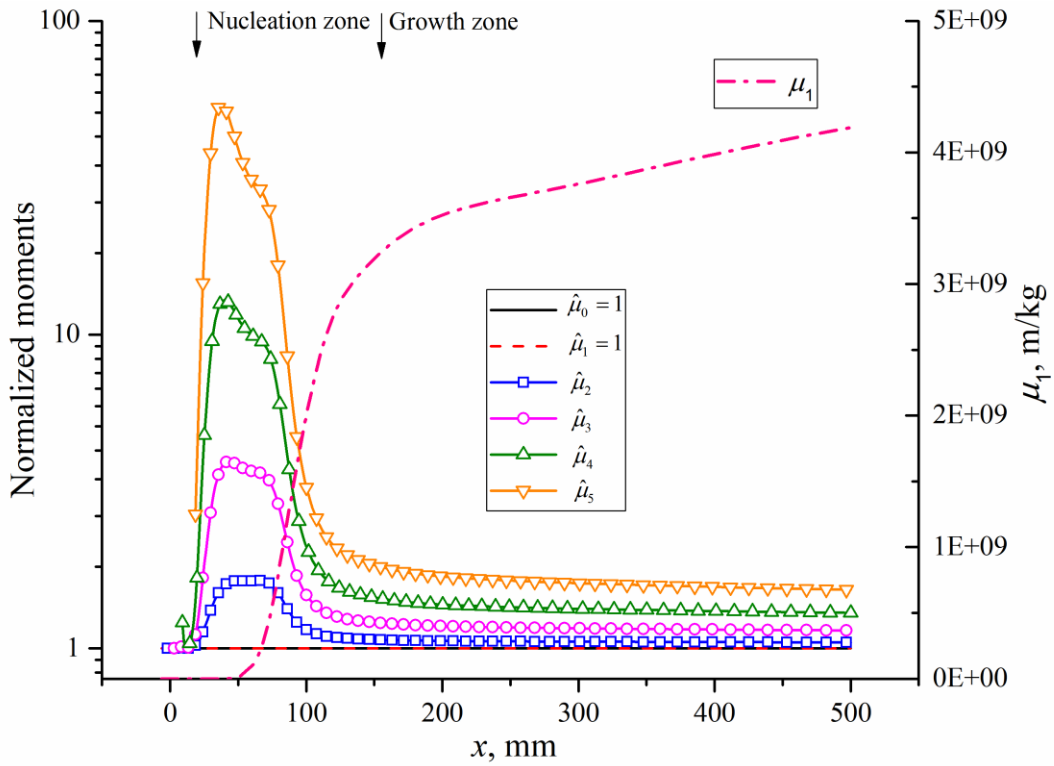

Fig. 30 Distributions of normalized moments at the axis of Moore nozzle B.

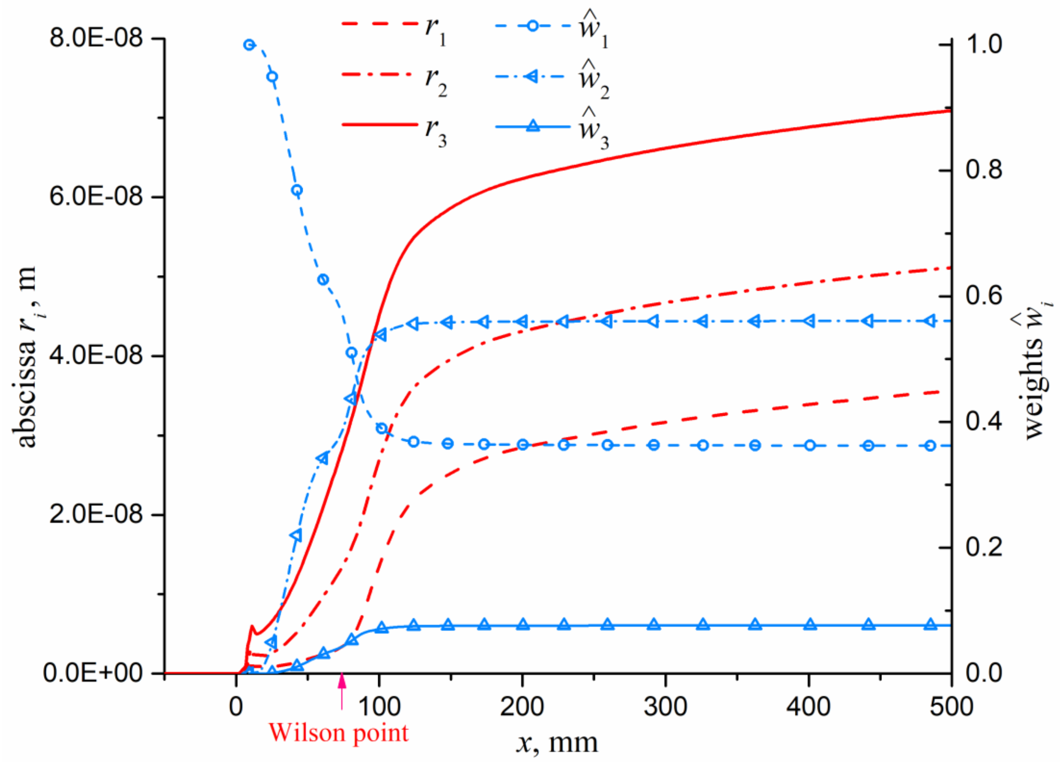

Fig. 31 Distributions of abscissa r_i and normalized weight w_i by PD algorithm for QMOM at the axis of Moore nozzle B.

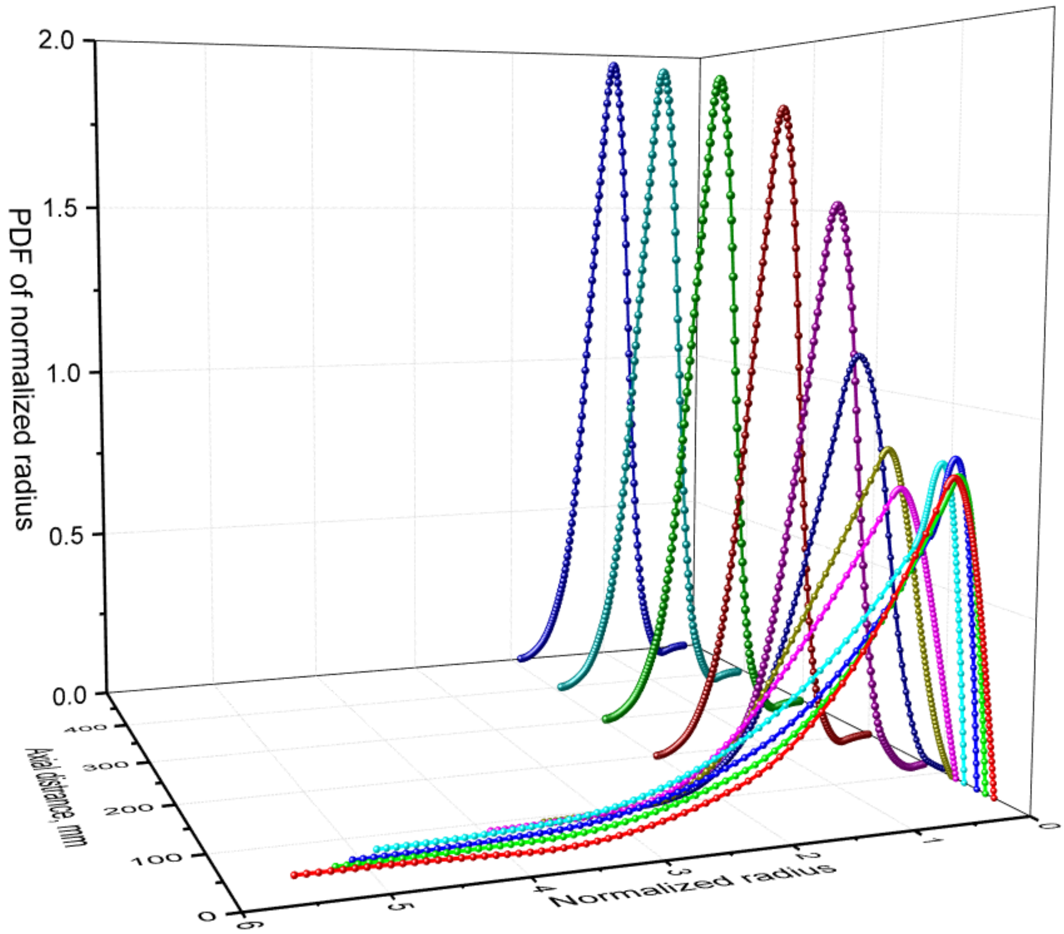

Fig. 32 Reconstructed PDF of normalized radius by using quadratic spline-based algorithm at different locations along the axis of Moore nozzle B.

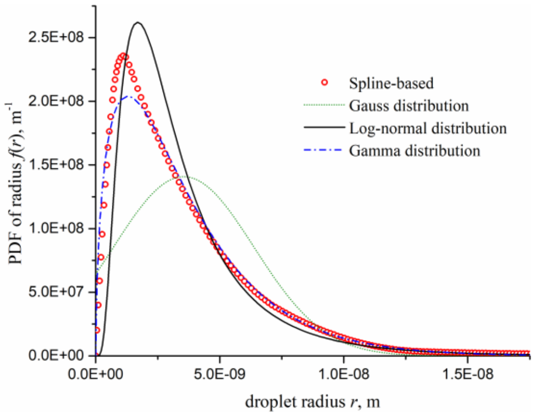

(a) $f(r)$ and weights at point C (50, 0)

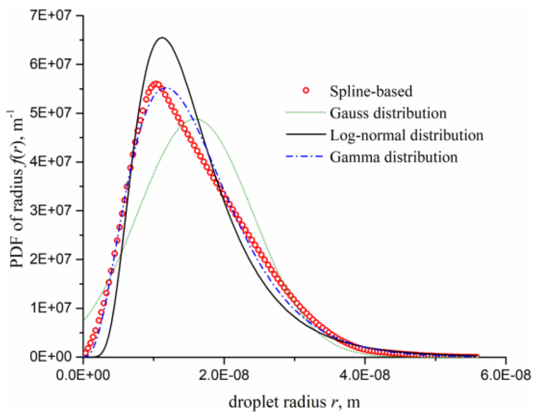

(b) f(r) and weights at point I (90, 0)

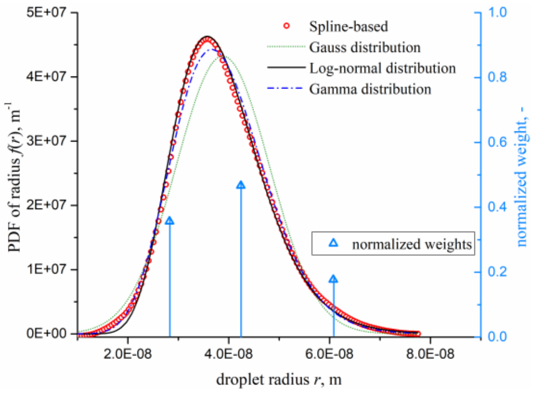

(c) $f(r)$ and weights at point L (200, 0)

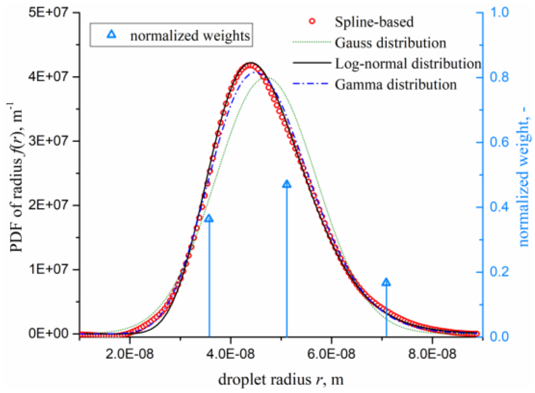

(d) $f(r)$ and weights at point O (500, 0)

Fig. 33 Reconstruction of probability density function $f(r)$ by using splined-based algorithm and priori shape functions from several moments at different locations along the axis of Moore nozzle B.

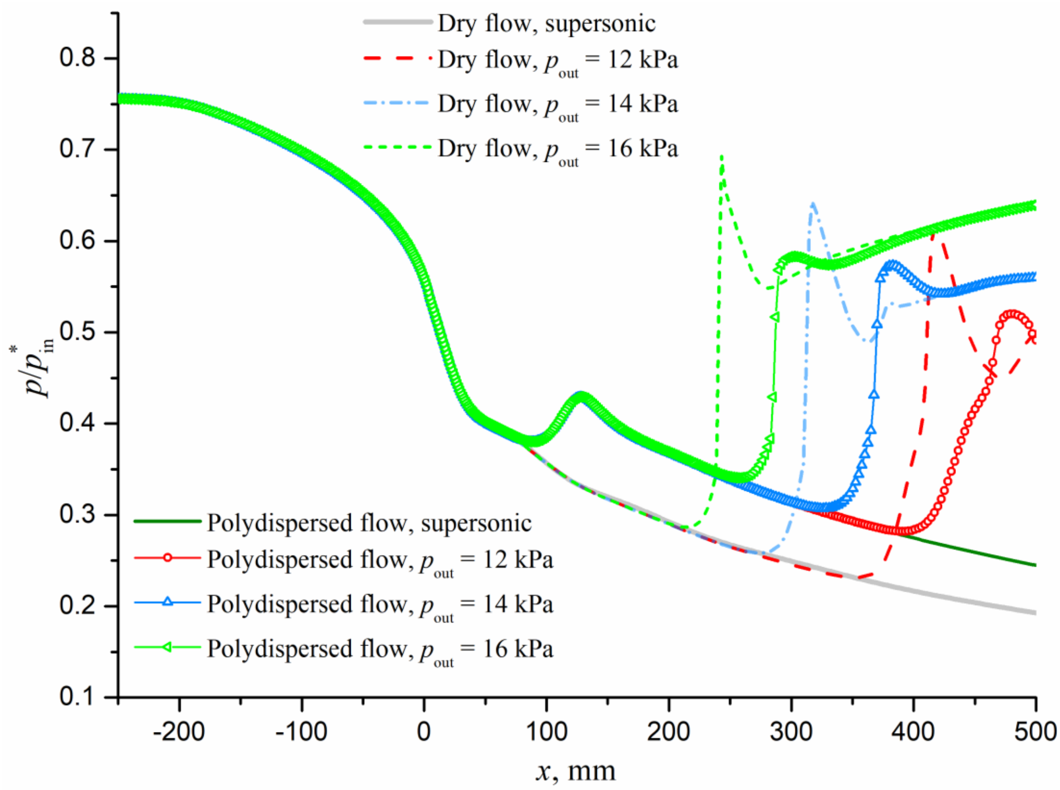

Fig. 34 Distribution of pressure ratio of polydispersed model with QMOM approach at the axis of Moore nozzle B with subsonic and supersonic outflows for dry and wet cases.

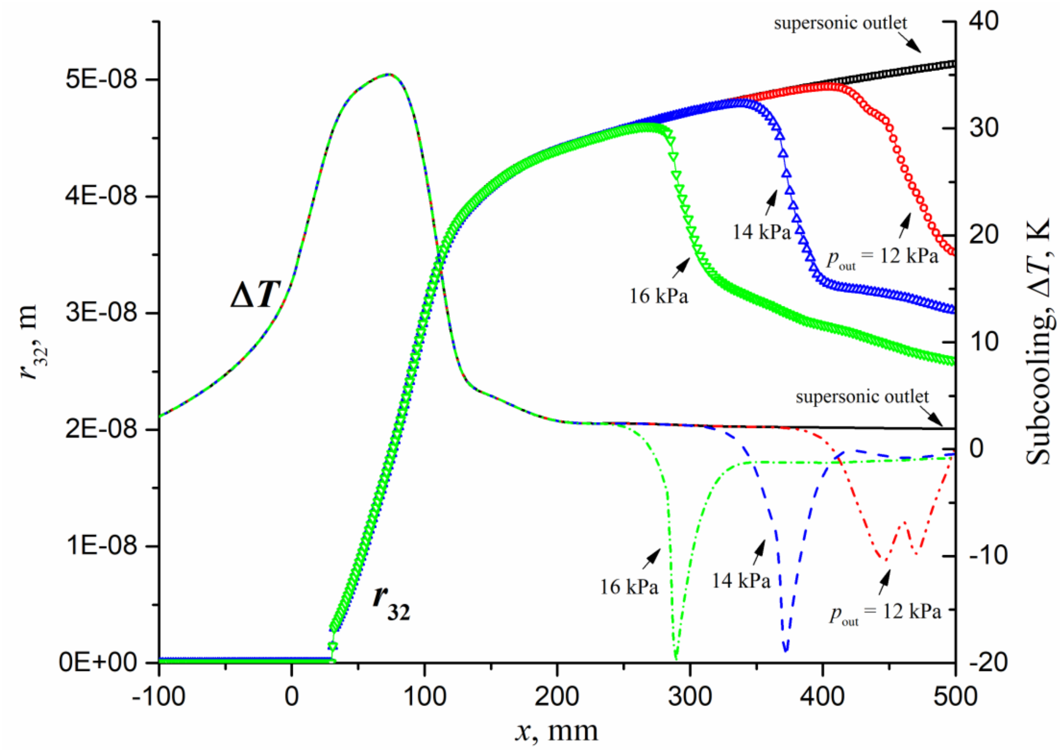

Fig. 35 The distributions of Sauter radius and wetness fraction of polydispersed model with QMOM approach at the axis of Moore nozzle B for various back pressures.

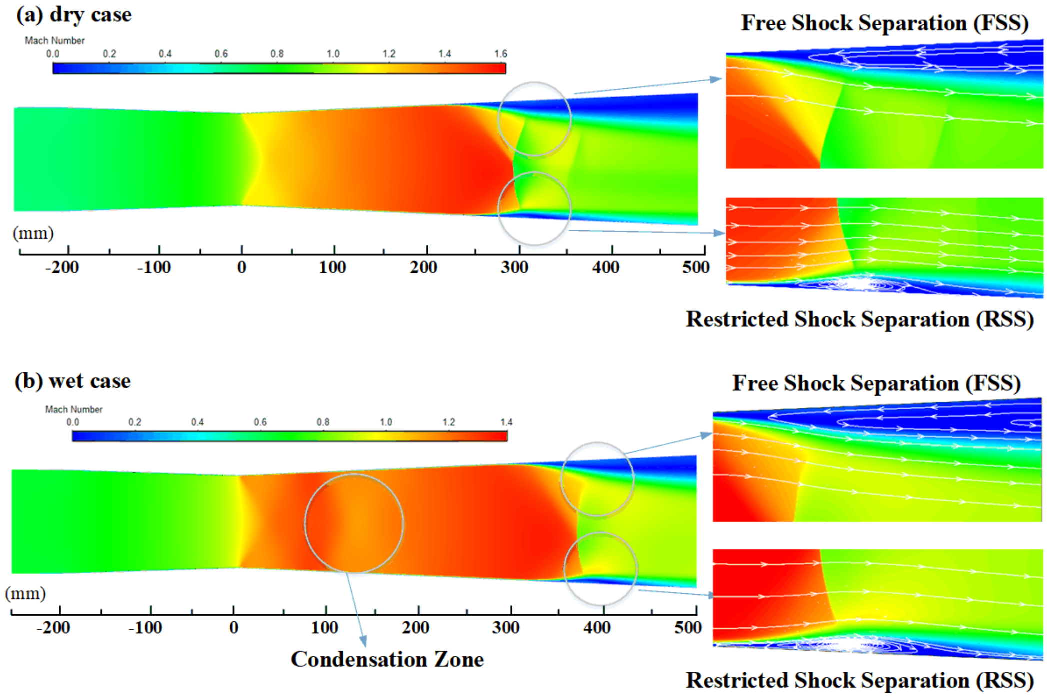

Fig. 36 Contours of Mach number and shock separation in Moore nozzle B: compared dry case (a) and wet case (b) when p_{out} = 14 kPa (subsonic outflow).

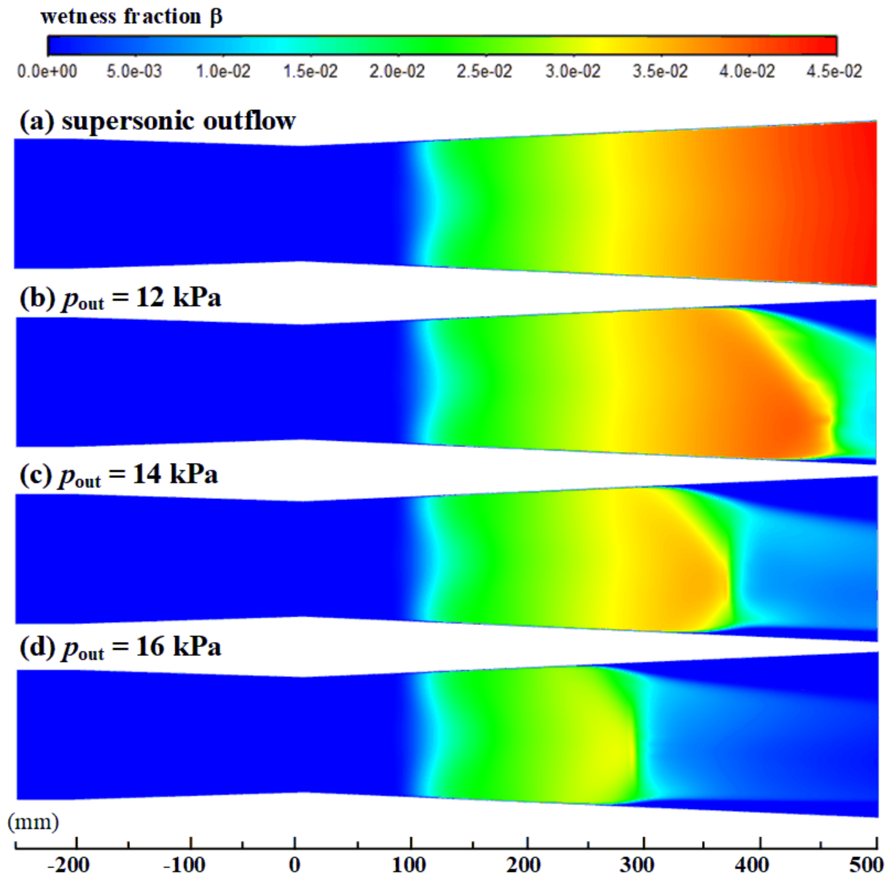

Fig. 37 Contours of wetness fraction in Moore nozzle B for various back pressures.

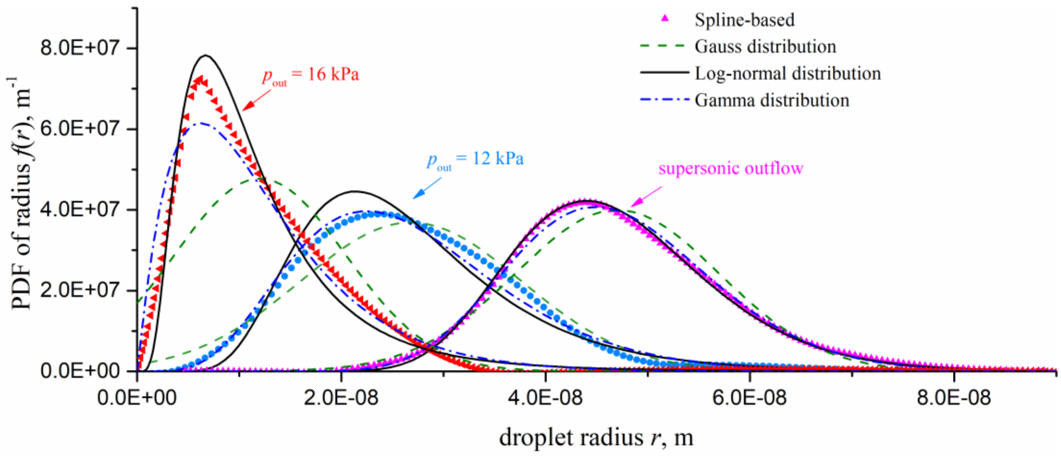

Fig. 38 Reconstructed $f(r)$ by splined-based algorithm and priori function shapes at nozzle outlet point O (500, 0) for various back pressure values.

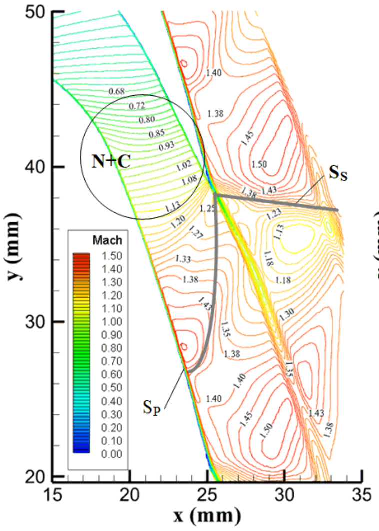

(a) Mach number

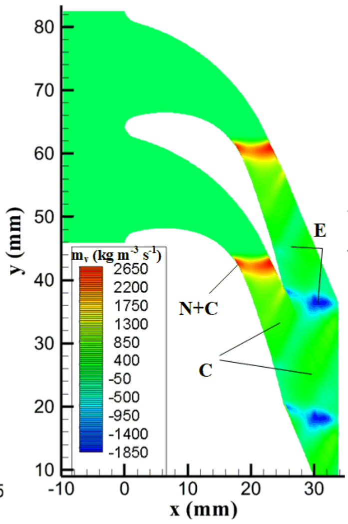

(b) mass change rate m_v

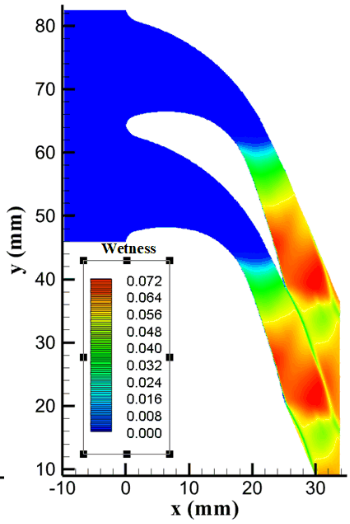

(c) wetness fraction β

Fig. 39 The contours of Mach number, mass change rate and wetness fraction of polydispersed model with QMOM approach in turbine blade for back pressure ratio p_{out}/p_{in}^* =0.30.

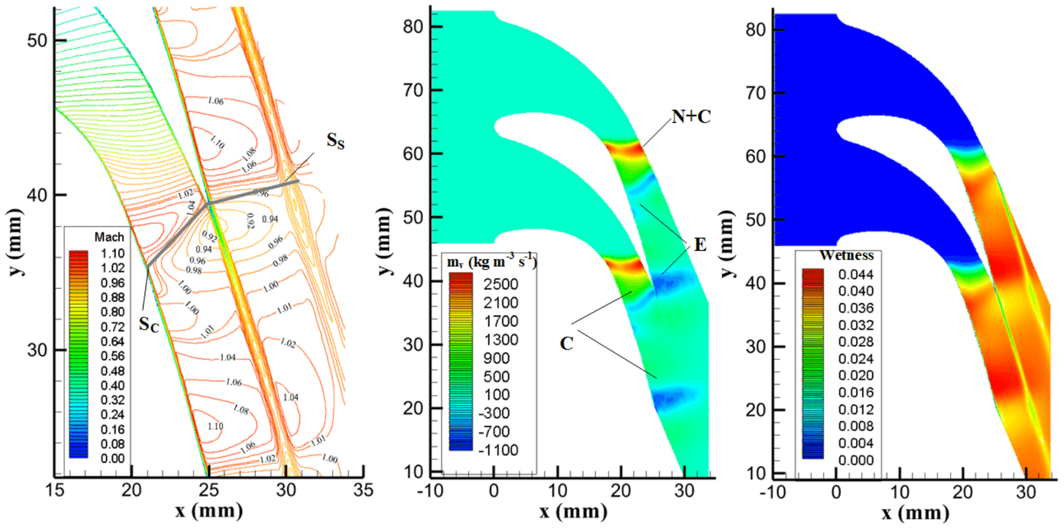

(a) Mach number (b) mass change rate m_v (c) wetness fraction β

Fig. 40 The contours of Mach number, mass change rate and wetness fraction of polydispersed model with QMOM approach in turbine blade for back pressure ratio p_{out}/p_{in}^{*} =0.50.

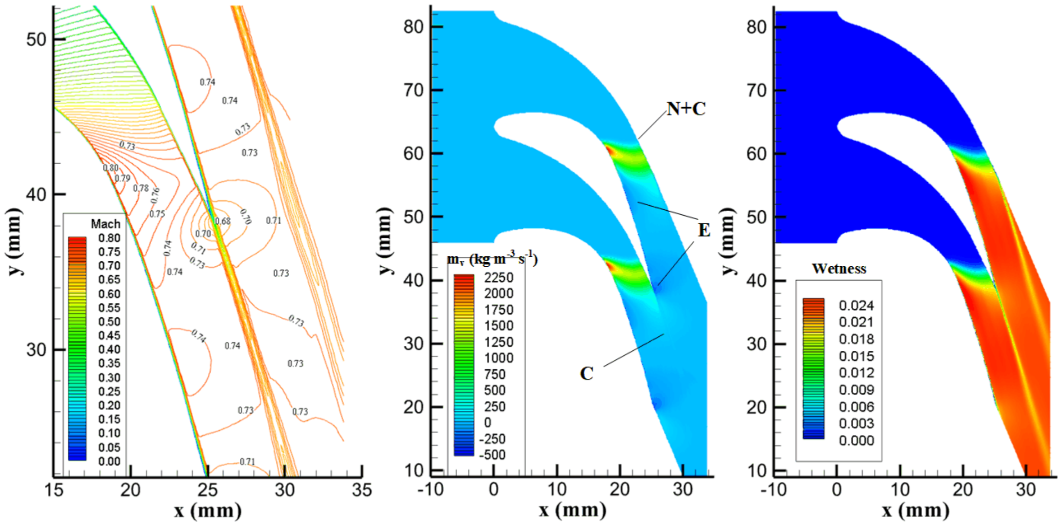

(a) Mach number (b) mass change rate m_v (c) wetness fraction β

Fig. 41 The contours of Mach number, mass change rate and wetness fraction of polydispersed model with QMOM approach in turbine blade for back pressure ratio p_{out}/p_{in}^{*} =0.70.

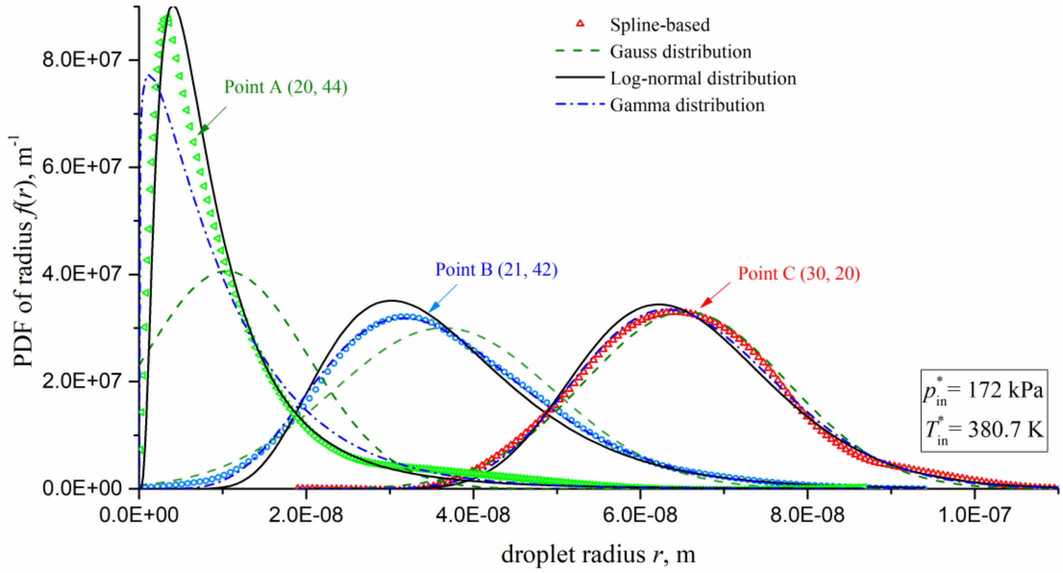

(a) at point A, B and C for the same back pressure p_{out}/p_{in}^* =0.30.

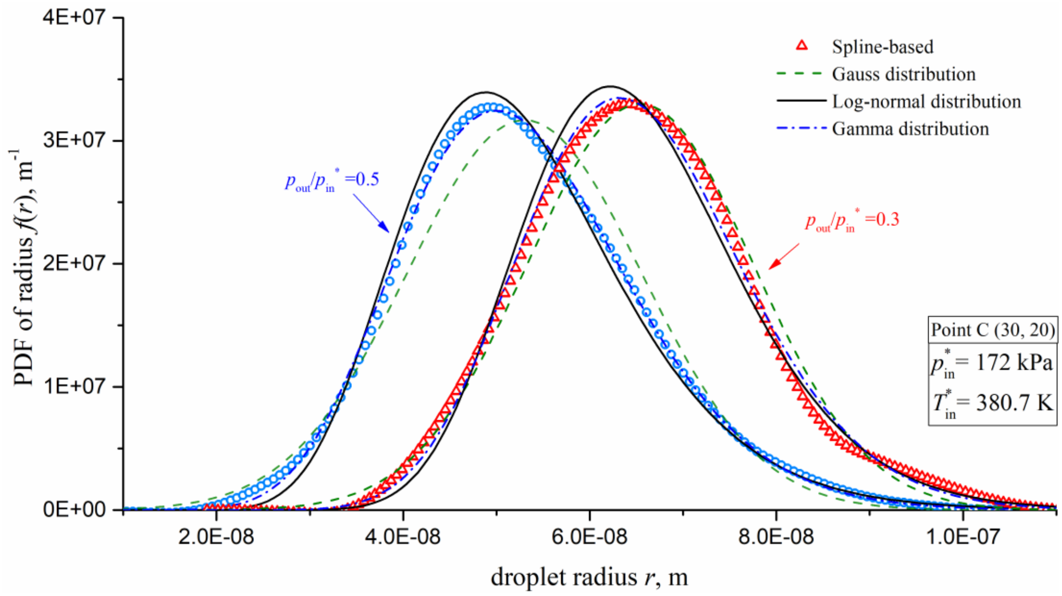

(b) at the same point for p_{out}/p_{in}^* =0.30 and 0.50.

Fig. 42 Reconstructed $f(r)$ by splined-based algorithm and priori function shapes from several moments in turbine blade.

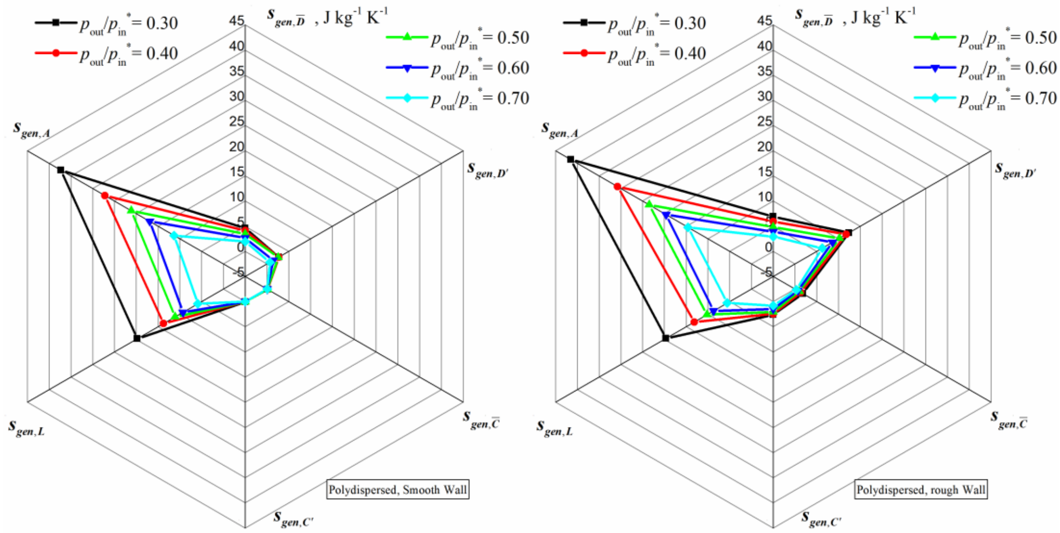

(a) with smooth wall (b) with rough wall

Fig. 43 Radar charts of multi-component entropy generations of wet steam flow of the polydispersed model with smooth and rough walls at different back pressures.

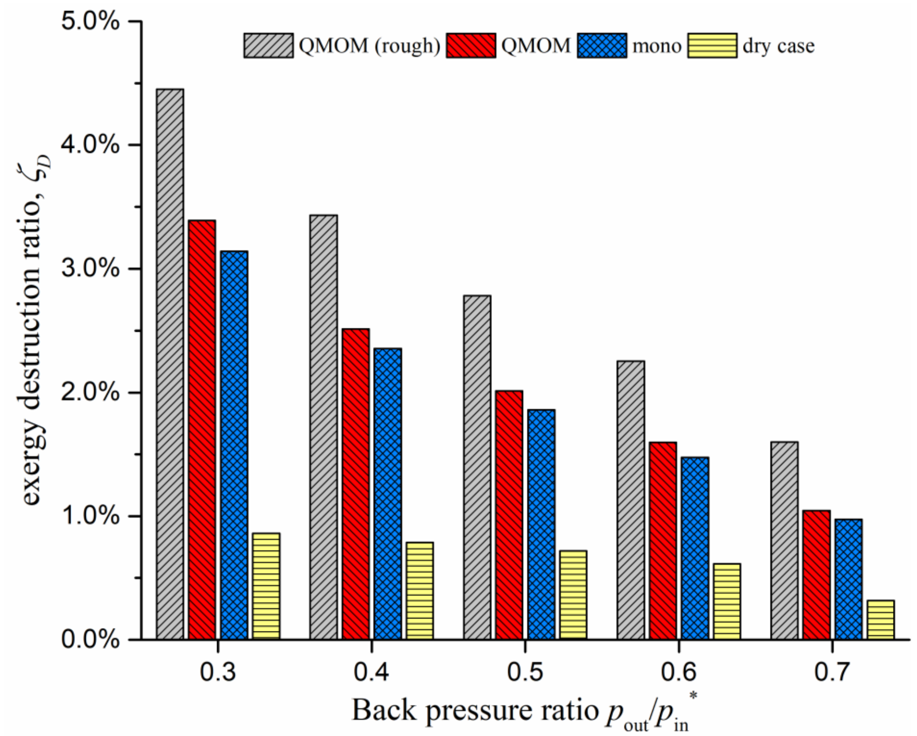

(a) Mass-weighted average of exergy destruction ratio ζ_D.

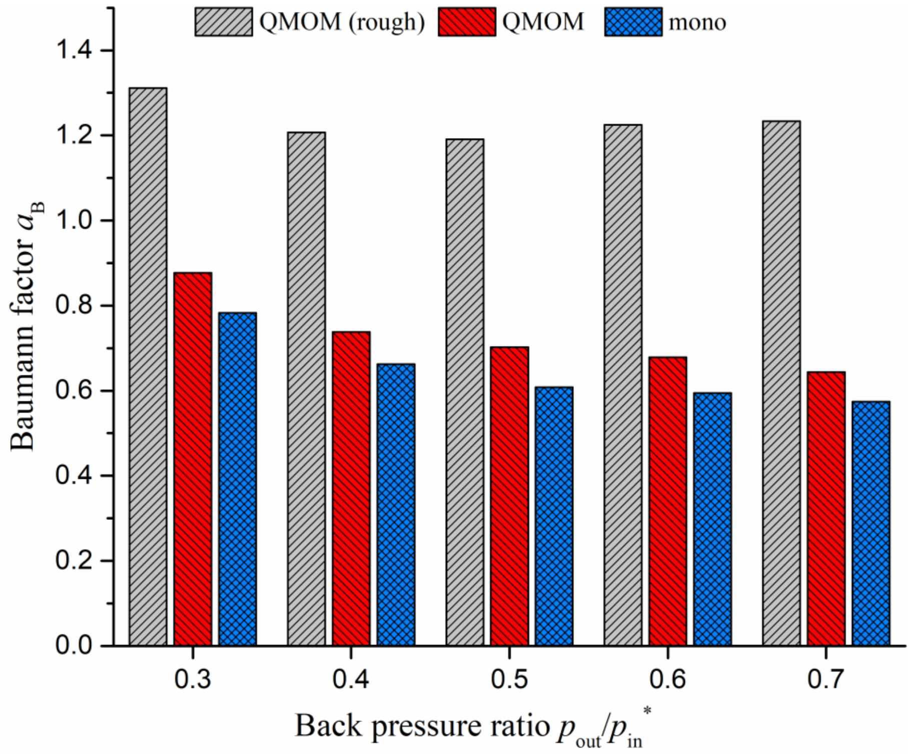

(b) Mass-weighted average of Baumann factor a_B.

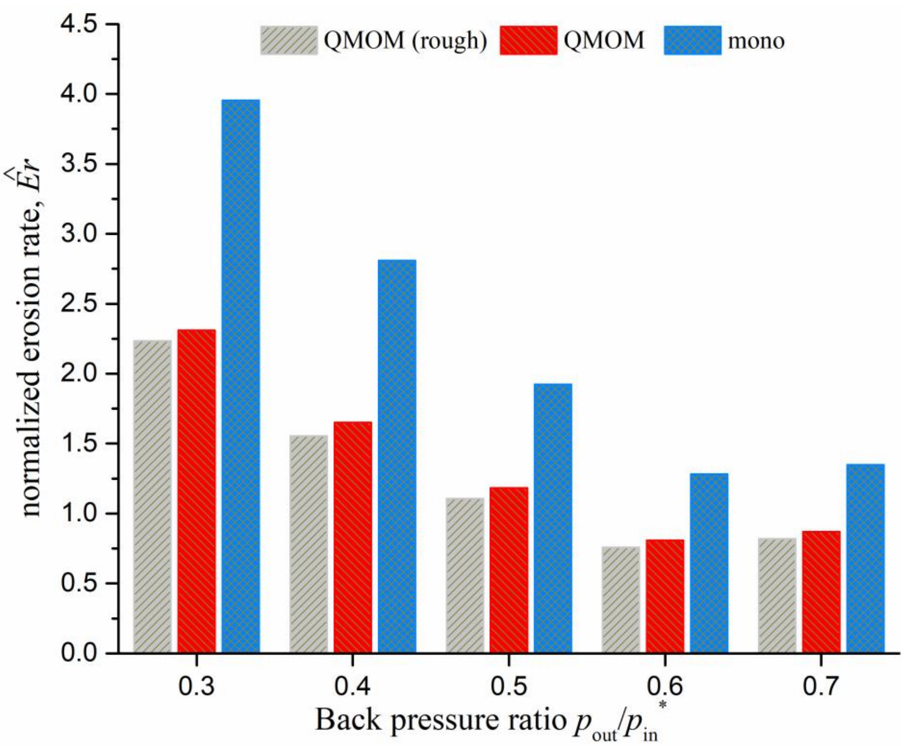

(c) Mass-weighted average of normalized erosion rate $\hat{Er}$

Fig. 44 The mass-weighted averages of exergy destruction ratio, Baumann factor and normalized erosion rate for wet and dry cases at different back pressure and wall roughness values.

Table 7 Boundary conditions of Moore nozzle B and Bakhtar turbine blade.

Experiments	p_{in}^*	p_{out}	T_{in}^*	$T_{s,in}$
Moore nozzle B	25 kPa	7 kPa(supersonic)	357.6 K	338.1 K
Bakhtar turbine blade	172 kPa	$0.48p_{in}^*$	380.66 K	388.66 K

Table 8 Geometry of Moore nozzle B.

Point	1	2	3	4
x	-250 mm	-200 mm	0 mm	500 mm
y	56.35 mm	56.35 mm	50.0 mm	72.0 mm

Table 9 Geometry of Bakhtar turbine blade.

Length	Chord	Pitch	Axial Chord	Inlet flow angle	Grid
76.00 mm	35.76 mm	18.26 mm	25.27 mm	0°	290 × 120

Table 10 Six moments and number-average radius at different locations along the axis of Moore nozzle B.

Point	x, mm	μ_0, kg^{-1}	μ_1, m kg^{-1}	μ_2, m^2 kg^{-1}	μ_3, m^3 kg^{-1}	μ_4, m^4 kg^{-1}	μ_5, m^5 kg^{-1}	r_{10}, m	C_V
A	30	5.57×10^{12}	7153.63	1.26×10^{-5}	3.51×10^{-14}	1.50×10^{-22}	8.59×10^{-31}	1.28×10^{-9}	0.609
B	40	4.26×10^{14}	8.89×10^{5}	2.96×10^{-3}	1.52×10^{-11}	1.06×10^{-19}	9.10×10^{-28}	2.09×10^{-9}	0.774
C	50	4.76×10^{15}	1.68×10^{7}	9.81×10^{-2}	8.09×10^{-10}	8.38×10^{-18}	1.02×10^{-25}	3.55×10^{-9}	0.779
D	60	1.85×10^{16}	9.90×10^{7}	0.86767	1.03×10^{-8}	1.49×10^{-16}	2.47×10^{-24}	5.34×10^{-9}	0.780
E	70	4.62×10^{16}	3.37×10^{8}	4.0084	6.35×10^{-8}	1.21×10^{-15}	2.61×10^{-23}	7.29×10^{-9}	0.794
F	75	6.40×10^{16}	5.33×10^{8}	7.0371	1.22×10^{-7}	2.50×10^{-15}	5.79×10^{-23}	8.32×10^{-9}	0.767
G	80	8.01×10^{16}	8.25×10^{8}	12.619	2.46×10^{-7}	5.61×10^{-15}	1.44×10^{-22}	1.03×10^{-8}	0.698
H	85	8.74×10^{16}	1.16×10^{9}	20.688	4.53×10^{-7}	1.15×10^{-14}	3.23×10^{-22}	1.32×10^{-8}	0.593
I	90	8.86×10^{16}	1.41×10^{9}	28.315	6.76×10^{-7}	1.84×10^{-14}	5.53×10^{-22}	1.59×10^{-8}	0.514
J	100	8.90×10^{16}	1.96×10^{9}	49.911	1.43×10^{-6}	4.52×10^{-14}	1.56×10^{-21}	2.21×10^{-8}	0.388
K	125	8.98×10^{16}	2.85×10^{9}	97.761	3.60×10^{-6}	1.42×10^{-13}	5.93×10^{-21}	3.17×10^{-8}	0.283
L	200	9.03×10^{16}	3.51×10^{9}	143.79	6.22×10^{-6}	2.83×10^{-13}	1.35×10^{-20}	3.88×10^{-8}	0.238
M	300	9.24×10^{16}	3.87×10^{9}	170.70	7.90×10^{-6}	3.83×10^{-13}	1.94×10^{-20}	4.19×10^{-8}	0.228
N	400	8.77×10^{16}	3.97×10^{9}	188.13	9.33×10^{-6}	4.84×10^{-13}	2.61×10^{-20}	4.53×10^{-8}	0.218
O	500	8.87×10^{16}	4.17×10^{9}	204.88	1.05×10^{-5}	5.62×10^{-13}	3.13×10^{-20}	4.70×10^{-8}	0.212

Table 11 Quadrature weights w_i and abscissa r_i calculated by PD algorithm of six normalized moments at point L (200 mm, 0 mm).

i	$\hat{\mu}_i$	$\hat{a}_i$	$\hat{b}_i$	$\hat{r}_i$	$\hat{w}_i$	r_i, m	w_i, kg^{-1}
0	1						
1	1	1	0.2376448	0.7281969	0.3565972	2.8265331×10^{-8}	3.2213845×10^{16}
2	1.0564750	1.1343497	0.3221083	1.0923890	0.4664764	4.2401628×10^{-8}	4.2139981×10^{16}
3	1.1770126	1.2512196		1.5649833	0.1769263	6.0745614×10^{-8}	1.5982959×10^{16}
4	1.3792684						
5	1.6950068						

Table 12 Mass-weighted average of entropy generations (J·kg^{-1}·K^{-1}) of blade outlet for the polydispersed, monodispersed and dry models at various back pressure ratio p_{out}/p_{in}^{*}.

p_{out}/p_{in}^{*}	Models	$s_{gen,\overline{D}}$	$s_{gen,D'}$	$s_{gen,\overline{C}}$	$s_{gen,C'}$	$s_{gen,L}$	$s_{gen,A}$	s_{gen}	e_D, kJ/kg
0.3	QMOM, rough	6.930	12.382	1.800	2.605	19.643	41.517	84.877	25.293
	QMOM	4.619	2.699	0.165	0.063	19.775	37.317	64.638	19.262
	Mono	4.663	2.605	0.170	0.092	22.723	29.641	59.895	17.849
	dry flow	6.525	3.131	0.384	0.909	0	5.480	16.428	4.896
0.4	QMOM, rough	5.947	11.782	1.355	2.454	13.153	30.755	65.446	19.503
	QMOM	4.139	2.692	0.127	0.050	13.737	27.186	47.932	14.284
	Mono	4.527	2.820	0.130	0.063	15.508	21.857	44.906	13.382
	dry flow	4.486	4.535	0.265	0.791	0	4.921	14.998	4.469
0.5	QMOM, rough	4.872	10.194	0.976	2.080	10.236	24.704	53.062	15.812
	QMOM	3.456	2.569	0.083	0.036	11.106	21.151	38.402	11.444
	Mono	3.706	2.443	0.088	0.023	11.940	17.261	35.459	10.567
	dry flow	4.073	5.484	0.191	0.796	0	3.157	13.701	4.083
0.6	QMOM, rough	3.913	8.596	0.654	1.474	8.712	19.619	42.969	12.805
	QMOM	2.677	1.436	0.059	0.006	9.299	16.938	30.415	9.064
	Mono	3.050	1.455	0.075	0.009	9.303	14.247	28.138	8.385
	dry flow	3.494	5.662	0.144	0.627	0	1.815	11.742	3.499
0.7	QMOM, rough	2.944	6.257	0.328	0.819	5.570	14.570	30.489	9.086
	QMOM	1.934	0.705	0.038	0.006	5.886	11.326	19.894	5.928
	Mono	2.139	0.744	0.039	0.007	5.908	9.725	18.562	5.532
	dry flow	2.662	2.709	0.080	0.232	0	0.355	6.038	1.799